

RESEARCH ARTICLE

# Thermal Transport Characteristics of Human Skin Measured *In Vivo* Using Ultrathin Conformal Arrays of Thermal Sensors and Actuators

R. Chad Webb<sup>1‡</sup>, Rafal M. Pielak<sup>2‡</sup>, Philippe Bastien<sup>3</sup>, Joshua Ayers<sup>1</sup>, Juha Niittynen<sup>4</sup>, Jonas Kurniawan<sup>1</sup>, Megan Manco<sup>5</sup>, Athena Lin<sup>1</sup>, Nam Heon Cho<sup>1</sup>, Viktor Malyrchuk<sup>1</sup>, Guive Balooch<sup>2,6\*</sup>, John A. Rogers<sup>1\*</sup>

**1** Frederick Seitz Materials Research Laboratory, Department of Materials Science and Engineering, University of Illinois at Urbana-Champaign, Urbana, Illinois, United States of America, **2** L'Oréal California Research Center, San Francisco, California, United States of America, **3** L'Oréal Research and Innovation, Aulnay sous Bois, France, **4** Tampere University of Technology, Department of Electronics and Communication Engineering, Korkeakoulunkatu 3, Tampere, Finland, **5** L'Oréal Early Clinical, Clark, New Jersey, United States of America, **6** L'Oréal Digital Incubator, Clark, New Jersey, United States of America

‡ These authors contributed equally to this work.

\* [gbalooch@rd.us.loreal.com](mailto:gbalooch@rd.us.loreal.com) (GB); [jrogers@illinois.edu](mailto:jrogers@illinois.edu) (JR)



OPEN ACCESS

**Citation:** Webb RC, Pielak RM, Bastien P, Ayers J, Niittynen J, Kurniawan J, et al. (2015) Thermal Transport Characteristics of Human Skin Measured *In Vivo* Using Ultrathin Conformal Arrays of Thermal Sensors and Actuators. PLoS ONE 10(2): e0118131. doi:10.1371/journal.pone.0118131

**Academic Editor:** Victor M Ugaz, Texas A&M University, UNITED STATES

**Received:** October 7, 2014

**Accepted:** January 5, 2015

**Published:** February 6, 2015

**Copyright:** © 2015 Webb et al. This is an open access article distributed under the terms of the [Creative Commons Attribution License](http://creativecommons.org/licenses/by/4.0/), which permits unrestricted use, distribution, and reproduction in any medium, provided the original author and source are credited.

**Data Availability Statement:** All relevant data are within the paper and its Supporting Information files.

**Funding:** RCW acknowledges support from the National Science Foundation under grant no. DGE-1144245 (<http://www.nsf.gov/>). JN acknowledges support from Tekes grant no: 40150/12 (<http://www.tekes.fi/>). The above funding sources had no role in study design, data collection and analysis, decision to publish, or preparation of the manuscript. Materials, instrumentation and human study costs were supported by L'Oréal Research & Innovation. RMP PB MM and GB are employed by L'Oréal and

## Abstract

Measurements of the thermal transport properties of the skin can reveal changes in physical and chemical states of relevance to dermatological health, skin structure and activity, thermoregulation and other aspects of human physiology. Existing methods for *in vivo* evaluations demand complex systems for laser heating and infrared thermography, or they require rigid, invasive probes; neither can apply to arbitrary regions of the body, offers modes for rapid spatial mapping, or enables continuous monitoring outside of laboratory settings. Here we describe human clinical studies using mechanically soft arrays of thermal actuators and sensors that laminate onto the skin to provide rapid, quantitative *in vivo* determination of both the thermal conductivity and thermal diffusivity, in a completely non-invasive manner. Comprehensive analysis of measurements on six different body locations of each of twenty-five human subjects reveal systematic variations and directional anisotropies in the characteristics, with correlations to the thicknesses of the epidermis (EP) and stratum corneum (SC) determined by optical coherence tomography, and to the water content assessed by electrical impedance based measurements. Multivariate statistical analysis establishes four distinct locations across the body that exhibit different physical properties: heel, cheek, palm, and wrist/volar forearm/dorsal forearm. The data also demonstrate that thermal transport correlates negatively with SC and EP thickness and positively with water content, with a strength of correlation that varies from region to region, e.g., stronger in the palmar than in the follicular regions.

contributed to study design, data analysis and writing of the paper.

**Competing Interests:** The authors RMP, PB, MM and GB are employed by L'Oreal, who also provides a portion of the funding for this work. This does not alter the authors' adherence to PLOS ONE policies on sharing data and materials.

## Introduction

Skin is the largest organ of human body and it provides one of the most diverse sets of functions. The outermost layer, the stratum corneum (SC), serves as a protective barrier and the first defense against physical, chemical and biological damage. The skin also receives and processes multiple sensory stimuli, such as touch, pain and temperature and aids in the control of body temperature and the flow of fluids in/out of the body [1]. These processes are highly regulated by nervous and circulatory systems, but also depend directly and indirectly on thermal characteristics. The thermal transport properties of this tissue system can reflect physical/chemical states of the skin, with potentially predictive value in contexts ranging from dermatology to cosmetology. Measurement systems for *ex vivo* analysis [2,3] have some utility in establishing a general understanding of the properties, but they are irrelevant to investigations of the skin as an integral part of a complex, living organism. Existing *in vivo* approaches couple the use of laser heating or induced changes in the temperature of the ambient with infrared thermography [4–6], or they exploit rigid probes that press against the skin [7,8]. These and other previously reported methods only apply to certain regions of the skin; they do not readily allow thermal mapping measurement or determination of anisotropic properties and they operate effectively only in controlled, laboratory settings. As a result, little information exists that quantitatively characterizes the relationships between the *in vivo* thermal transport properties of skin and clinically relevant parameters such as hydration, vascularization and structure. Here, we introduce strategies that exploit ultrathin, soft systems [9–18] of thermal actuators and sensors for robust, precise transport measurements, in a non-invasive manner that can rapidly capture both orientation and position dependent characteristics. Assessments of the skin at six different body locations in twenty-five human subjects illuminate systematic variations in both the thermal conductivity and thermal diffusivity, for which measurements by optical coherence tomography (OCT), and electrical impedance yield additional insights into the underlying physiology.

Our recent report [10] introduced a type of thermal sensor with thickness, modulus and thermal mass matched to the epidermis, for spatiotemporal mapping of temperature on the surface of the skin with precision equal to or better than that of state-of-the-art infrared thermography systems. In the present work, advanced versions of this technology enable mapping of not only temperature but also thermal transport properties, including thermal conductivity and thermal diffusivity (and, therefore, the heat capacity per unit volume via the ratio of these two quantities) and their in-plane directional anisotropies. A representative device, shown in Fig. 1a and b mounted on the cheek, consists of a 4×4 array of interconnected filamentary metal structures (Cr/Au; 6/75 nm thick, 10 μm wide) that simultaneously function as thermal sensors and actuators, where the temperature coefficient of resistance of the metal couples changes in temperature to changes in resistance. A thin (<3 μm) film of polyimide encapsulates these structures and their electrical interconnects (Ti/Cu/Ti/Au; 10/500/10/25 nm thick, 50 μm wide) both above and below. A low modulus (35 kPa), thin coating (as small as 5 μm) of a silicone elastomer (Ecoflex 00–30, Smooth-on, USA) provides a conformal, intimate thermal interface directly to the SC. This soft mode of contact, together with the stretchable construction of the overall system, allows for repeated cycles of application, operation and removal without adverse effect on the device or the skin. The maximum heating powers used in experiments reported here introduce readily measurable changes in the temperature at the surface of the skin, but at levels that lie below the human sensory threshold. Optical coherence tomographic (OCT; VivoSight, Michelson Diagnostics, UK) images (Fig. 1c and d) of a region of the skin before and after mounting the device (highlighted in blue) highlight the high level of conformal contact afforded by soft, compliant construction. A wired electrical interface to a USB-

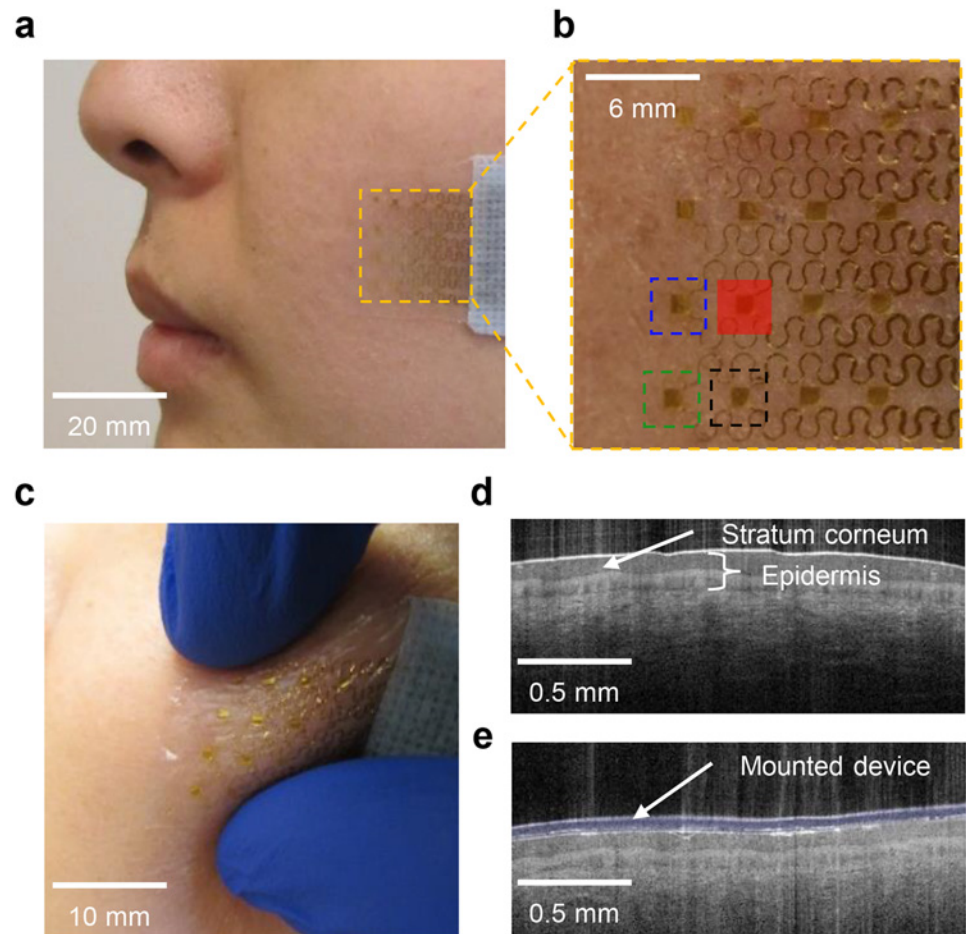


**Fig 1. Ultrathin, conformal device for evaluating thermal transport characteristics and validation on human skin.** (a) Photograph of a device laminated onto a subject's cheek. (b) Magnified view showing the location of the heater (red), a sensing element 3.5 mm away from the heater (blue), 4.7 mm away (black), and 5.8 mm away (green). (c) Magnified view during deformation. (d) Optical coherence tomography image of a region of a human palm before and (e) after mounting the array (blue).

doi:10.1371/journal.pone.0118131.g001

powered portable data acquisition system enables operation in non-laboratory settings. See [S1 Notes 1–2](#) and [S1–S4 Figs](#) for device fabrication and data acquisition details, and statistical analysis of *in vivo* device temperature readings compared to infrared techniques.

## Results

The sensors and actuators can be used interchangeably in two different modes to assess thermal transport. The first mode uses each element in the array sequentially and independently as both an actuator and a sensor. The measurement occurs quickly ( $<2$  s), with capabilities for spatial mapping. An infrared image collected during the heating sequence ([Fig. 2a](#)) shows results of local, rapid heating generated by a single element. [Fig. 2b](#) illustrates findings from FEM modeling of the 3-dimensional temperature distribution after 1.2 s of heating, to provide a sense of the depth and lateral spatial scales associated with the measurement. For routine analysis, a simple modification to an analytical treatment [[19](#)] in which the heating element is

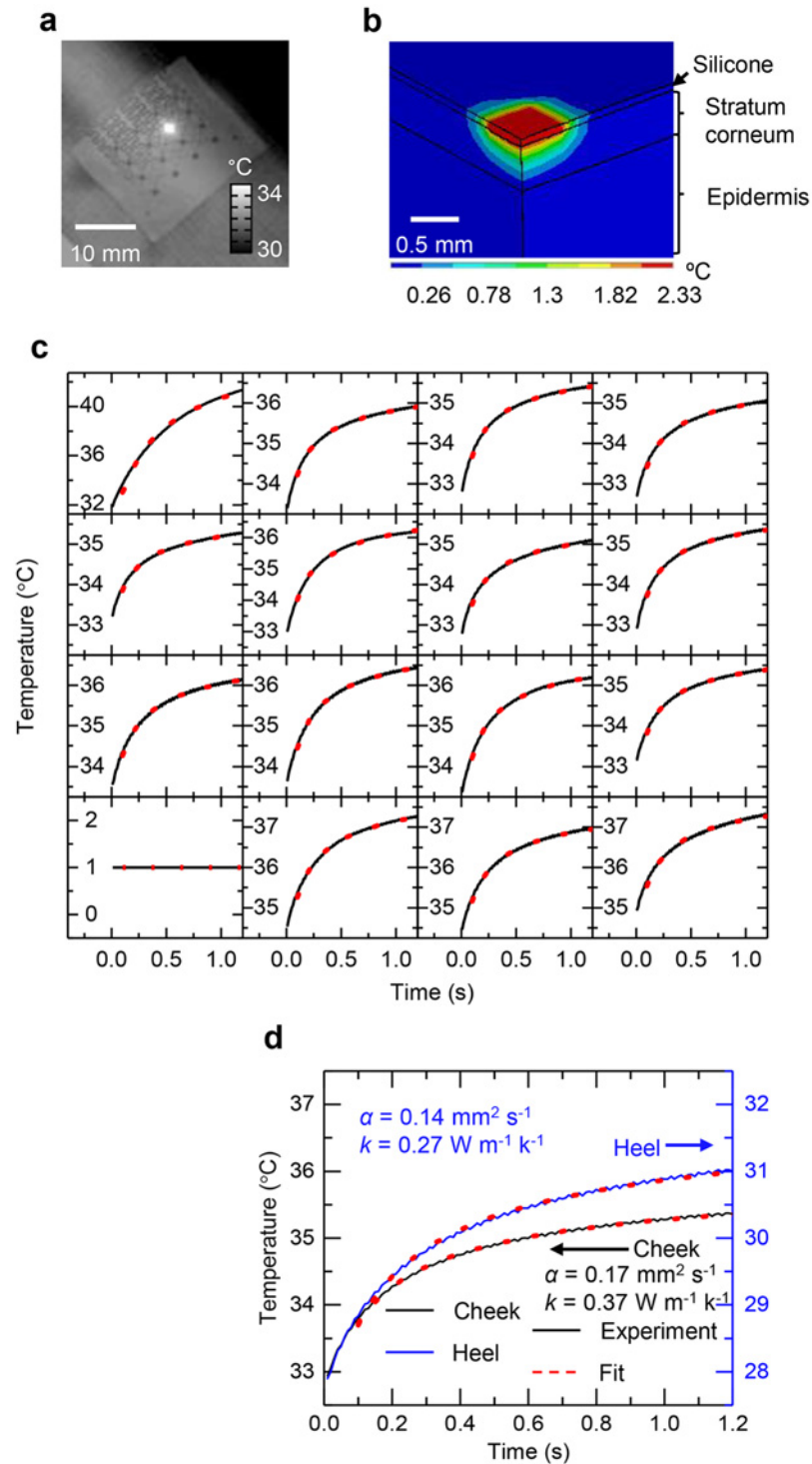


**Fig 2. Thermal flow associated with low level transient heating on the surface of the skin.** (a) Infrared image during heating at a single thermal actuator in an array device on the skin. (b) Finite element modelling results for the distribution of temperature during rapid, low level heating at an isolated actuator on the skin, after 1.2 s of heating at a power of  $3.7 \text{ mW mm}^{-2}$ . (c) Spatial map of the rise in temperature due to transient heating sequentially in each element in the array. The solid black lines are experimental data; the red dashed lines are best fit calculations. The strong rise shown in upper leftmost element results from local delamination of the device from the skin. (d) Experimental data (solid lines) and best fit calculations (dashed lines) for the cheek (black) and heel (blue), along with extracted thermal transport properties.

doi:10.1371/journal.pone.0118131.g002

considered as a point heat source in a semi-infinite plane can be valuable. Here,

$$T = T_{\infty} + A_1 \frac{Q}{2\pi A_2 k_{skin}} \operatorname{erfc} \left( \frac{A_2 \sqrt{\rho_{skin} c_{p,skin}}}{\sqrt{4k_{skin} t}} \right) \quad (1)$$

where  $T$  is the temperature at an effective distance,  $A_2$ , from the heater,  $T_{\infty}$  is the temperature before heating,  $Q$  is the heating power,  $k_{skin}$  is the thermal conductivity of the skin,  $\rho_{skin} c_{p,skin}$  is the volumetric heat capacity of skin,  $t$  is time, and  $\operatorname{erfc}$  is the complementary error function.  $A_1$  is a parameter that accounts for details associated with the multilayered geometry of the device; its value is calibrated through measurements of materials with known thermal properties similar to those of the skin (water, ethylene glycol and polydimethylsiloxane).  $A_2$  accounts for the fact that the thermal actuator (serpentine wire distributed over an area of  $1 \times 1 \text{ mm}^2$ ) when used as a sensor records a temperature that corresponds to a weighted average over the area of the element. This average temperature, in the model of equation (1), is equivalent to the value at a distance  $A_2$  away from an effective point source of heat. As a result,  $A_2$  lies between 0 and 0.5 mm, depending on the geometric details and materials properties. In practice,  $A_2$  is selected to yield quantitatively accurate results with materials of known thermal properties similar to those of skin. Analysis of *in vivo* data involves an iterative fitting procedure (Matlab, Mathworks, USA) to determine  $k_{skin}$  and the thermal diffusivity ( $\alpha_{skin} = \rho c_{p,skin} / k_{skin}$ ) using equation (1). Analyses of the sensitivity of the fitting process in the presence of experimental noise indicate maximum uncertainties of 2% and 8% for  $k_{skin}$  and  $\alpha_{skin}$ , respectively (S1 Notes 3 and S5 Fig). A similar analysis for errors in sensor calibration indicate maximum uncertainties of 5% and 15%. Measurements described subsequently demonstrate *in vivo* repeatability of better than 6% and 9% for  $k_{skin}$  and  $\alpha_{skin}$  respectively. Comparison of thermal properties determined using equation (1) to those determined using solutions that explicitly integrate numerically over the sensor area indicate discrepancies that lie below the level of these experimental errors (S1 Notes 4).

Examples of representative data (black lines) and calculations based on equation (1) (red dashed lines) for each element across the array appear in Fig. 2c (an example of a malfunctioning sensor that can be quickly identified by the lack of signal, and removed from analysis, is seen in the bottom-most, left-most graph). Fig. 2d presents similar results along with extracted values of  $k_{skin}$  and  $\alpha_{skin}$  for the cheek and the heel pad. The differences between these two cases are significant, and likely result, at least in part, from the variations in the thicknesses of the SC, as described subsequently. The effective depth associated with the measurement can be approximated as [20]

$$\Delta_p = \sqrt{\alpha t_{max}} \quad (2)$$

where  $t_{max}$  is the characteristic measurement time. This equation gives a probing depth of ~0.5 mm which agrees well with experimental analysis of measurement depth (S1 Notes 5, S6 Fig) as well as the depth of heating shown by the FEM results in Fig. 2b. The depth dependent properties of the skin over this length scale influence the measurements.

This measurement mode enabled comprehensive, systematic studies of thermal transport characteristics, *in vivo*, on twenty-five human subjects at six different body locations: cheek, dorsal forearm (d-forearm), volar forearm (v-forearm), volar wrist, palm and heel pad. Results for  $k_{skin}$  and  $\rho_{skin} c_{p,skin}$  follow from analysis using equation (1);  $\alpha_{skin}$  which corresponds to their ratio, is useful to consider also, because it determines whether  $k_{skin}$  and  $\rho_{skin} c_{p,skin}$  vary independently across body locations. Correlations between skin thermal properties to SC hydration measured using a corneometer (Cutometer MPA 580, Courage + Khazaka Electronics GmbH), EP thickness and SC thickness measured using OCT provide further insights into the

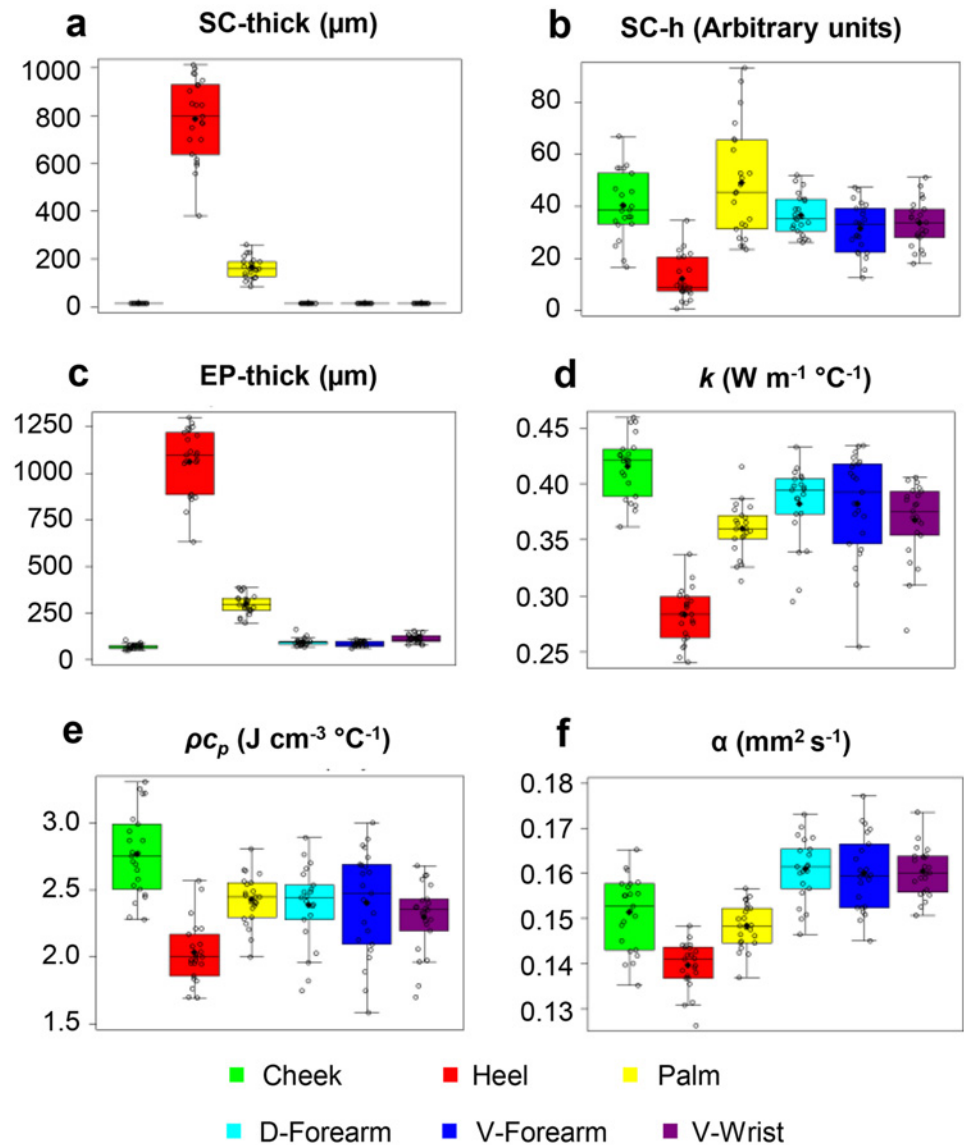


**Fig 3. Clinical data distributions.** Boxplot representation of the data (open circles). The mean is represented by a black diamond shape. The top and the bottom line of the box are the first and third quartiles, and the middle line of the box is the second quartile—the median. The lower (upper) whisker represents the minimum (maximum) observation above (below) the 1.5 Inter Quartile Range (IQR) below (above) the lower (upper) quartile. Data distributions for the (a) stratum corneum thickness (SC-thick), (b) stratum corneum hydration (SC-h), (c) epidermis thickness (EP-thick), (d) thermal conductivity ( $k$ ), (e) volumetric heat capacity ( $\rho c_p$ ), and (f) thermal diffusivity ( $\alpha$ ).

doi:10.1371/journal.pone.0118131.g003

results. Fig 3, which shows the distribution of these variables using a boxplot representation, reveals three distinct clusters for the thermal parameters: 1 cheek; 2 heel; and 3 palm, wrist, v-forearm and possibly d-forearm (the spread in the data here is relatively large due to the interference of hair on the measurement). Some separation occurs between the palm and the wrist/v-forearm/d-forearm, but to a degree that is not apparent from the univariate descriptive analysis. OCT yielded accurate values of SC thickness for the palm and heel pad but not for the follicular regions, where previous studies indicate a typical value of  $\sim 15 \mu\text{m}$  [21–23].

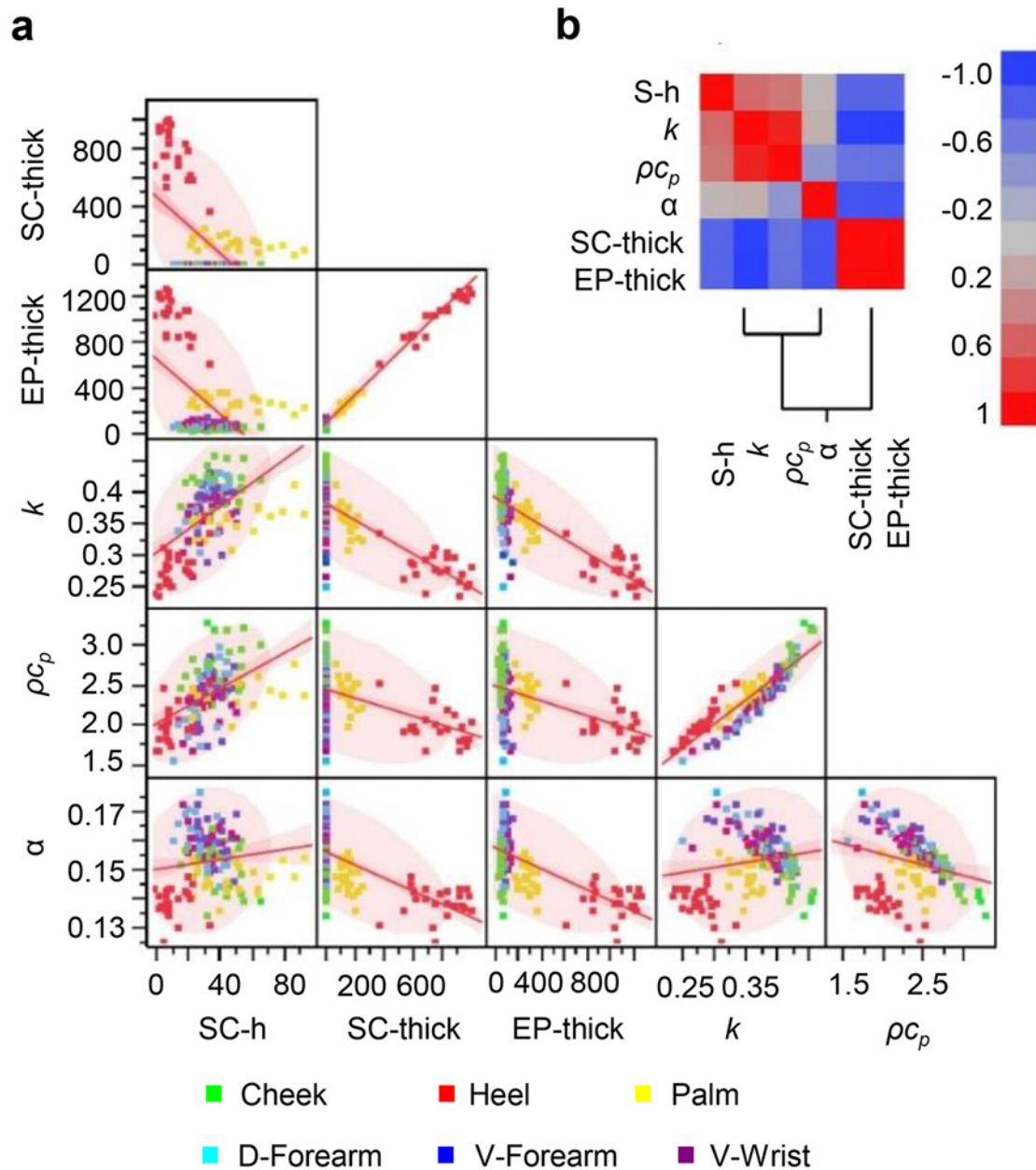


**Fig 4. Clinical data correlation analysis.** (a) Scatterplot matrix representation for the entire data set (all 6 body locations: cheek, volar and dorsal forearm, wrist, palm, and heel on 25 total subjects). Pairwise correlation analyses include the thermal characteristics ( $k$ ,  $W\ m^{-1}\ ^\circ C^{-1}$ ;  $\rho c_p$ ,  $J\ cm^{-3}\ ^\circ C^{-1}$ ;  $\alpha$ ,  $mm^2\ s^{-1}$ ) and stratum corneum thickness (SC-thick,  $\mu m$ ), epidermal thickness (EP-thick,  $\mu m$ ), and stratum corneum hydration (SC-h, arbitrary units). Data for different body areas are represented by different colors. The red line represents the pairwise linear regression slope. The pink shaded clouds represent the 95% bivariate normal density ellipse. Assuming the variables are bivariate normally distributed, this ellipse encloses approximately 95% of the points. (b) The bivariate correlations for the entire data set are represented using a color coding (HeatMap) scheme associated with a clustering of the descriptors. Dark red is associated with Pearson Correlation Coefficient,  $R$ , equal to 1 and dark blue is associated to  $R = -1$ . The Pearson correlation coefficients are given in [S1 Table](#).

doi:10.1371/journal.pone.0118131.g004

Pairwise correlation analyses for the skin thermal parameters, SC and EP thickness, and SC hydration appear in [Fig 4](#) for the entire data set, in [Fig 5](#) for each follicular region and in [Fig 6](#) for the palm and heel pad. The data show strong positive correlation between SC hydration and  $k_{skin}$  and  $\rho_{skin}c_{p,skin}$ . The ratio  $\alpha_{skin}$  exhibits a positive, but weaker, correlation with SC

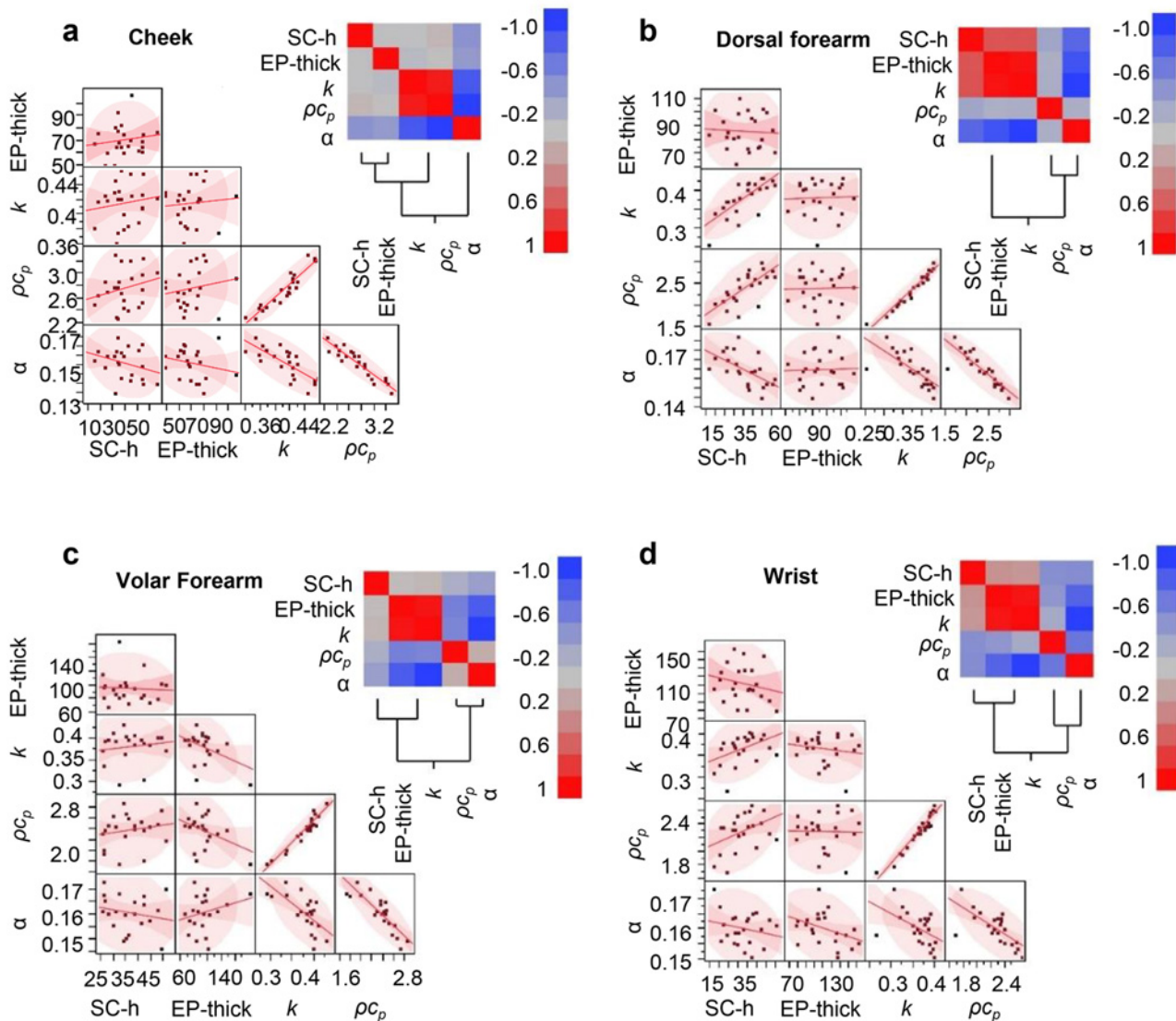


**Fig 5. Clinical data correlation analysis for regions without significant stratum corneum thickness.** The same correlation analysis as in Fig. 6 for the (a) cheek, (b) dorsal forearm, (c) volar forearm and (d) wrist.

doi:10.1371/journal.pone.0118131.g005

hydration. The data also indicate a strong negative correlation between SC/EP thickness and all three thermal properties ( $k_{skin}$ ,  $\rho_{skin}c_{p,skin}$  and  $\alpha_{skin}$ ). The EP thickness correlates with the SC thickness. SC is a significant fraction of the EP, especially in palmar regions, i.e. palm and heel pad. The SC thickness and SC hydration of the palmar regions show negative correlation. The strength of correlation depends strongly on body location (Figs. 5 and 6, and S1 Table).

Principal component analysis (PCA), as a global multivariate approach of correlation analysis, appears in Fig. 7 and S8 Fig. PCA offers a graphical representation of both individuals and descriptors, with an ability to reveal hidden patterns in the data. The eigenvalues show that the first PCA axis explains 71% of the variance. The second and third components correspond to 20% and 7%, respectively. Hence, three components explain 97% of the inertia. In the biplot representation, the data, by location, are represented using scores coordinates, where the scores are the Principal Components (PCs). The first PC mainly separates observations of the heel

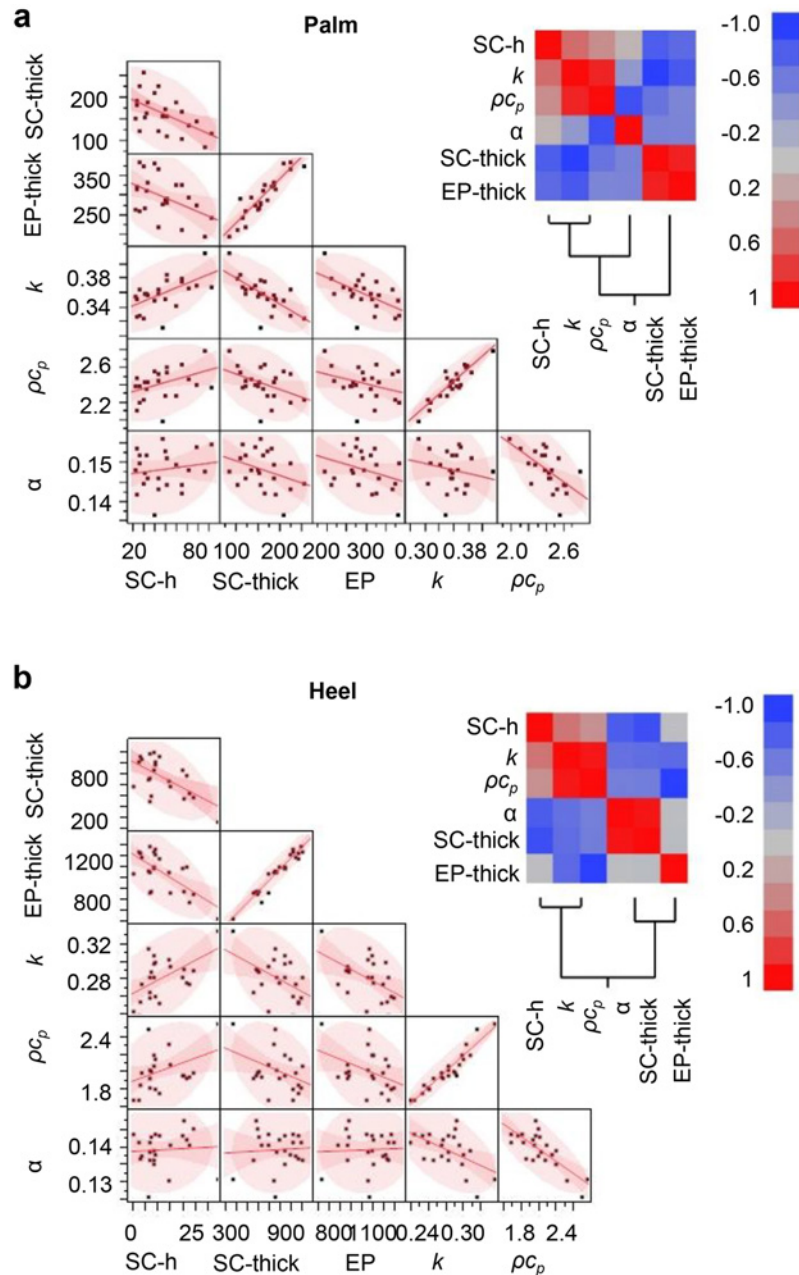


**Fig 6. Clinical data correlation analysis for regions with significant stratum corneum thickness.** The same correlation analysis as in Fig. 6 for the (a) palm and (b) heel.

doi:10.1371/journal.pone.0118131.g006

from the other body areas (Fig. 7 and S8a Fig). Discrimination also occurs, to a lesser extent, between the cheek and a group composed of palm, v-forearm, d-forearm and wrist (S8a Fig). The second PC discriminates the arm and wrist location from the others (S8b Fig). The third PC differentiates the palm (S8c Fig). Based on the PCs, four distinct clusters occur within the data set: heel, cheek, palm, and wrist/v-forearm/d-forearm indicating four distinct locations with different physical properties. Descriptors close together on the biplot are highly correlated and conversely descriptors opposed are highly anti-correlated. On the biplot, SC hydration, thermal conductivity and volumetric heat capacity form one group and EP thickness and SC

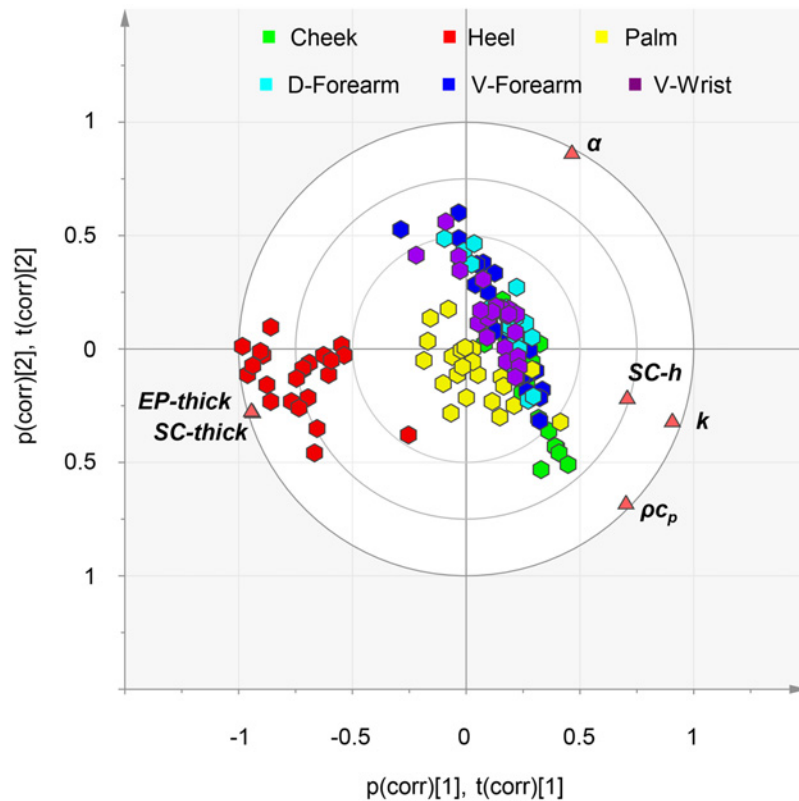


**Fig 7. Principal Component Analysis.** Global, multivariate correlation analysis. On the Biplot each body location is represented by polygons and the descriptors by triangles.

doi:10.1371/journal.pone.0118131.g007

thickness for another with the two groups opposed on the first axis. This conveys the strong positive correlation of descriptors from the same group and conversely the negative correlation of descriptors from different groups. Interestingly, the thermal diffusivity is more linked to the second axis, and therefore quite independent to the other descriptors. This is consistent with previous remarks based on Pearson correlation coefficients.

In addition to intrinsic properties of the skin itself, a second mode for characterizing thermal transport allows investigation of directional anisotropies and other effects related, for example, to blood flow near surface arteries and veins. Here, application of electrical power ( $8 \text{ mW} / \text{mm}^2$  for 60 s) to a selected element (highlighted by the red box in Fig. 2b (optical image) and Fig. 8a (data)) introduces a controlled level of heating while the temperature of this element and all others in the array are simultaneously recorded as a function of time. Processing the data with an adjacent-averaging filter (window size = 8 s), and subtracting the response of the sensor furthest from the actuator (Element 16) from that of each of the other sensors in the array minimizes effects of fluctuations in the ambient temperature. Here, the actuator can be approximated as a point source of heat, such that the transient temperature profile at a distance  $r$  can be written

$$T = T_{\infty} + A_1 \frac{Q}{2\pi r(t)k_{skin}} \operatorname{erfc} \left( \frac{r(t)\sqrt{\rho_{skin}c_{p,skin}}}{\sqrt{4k_{skin}t}} \right) \quad (3)$$

where  $T_{\infty}$  is the temperature before heating,  $Q$  is the heating power,  $k_{skin}$  is the thermal conductivity of the skin,  $\rho_{skin}c_{p,skin}$  is the volumetric heat capacity of skin,  $t$  is time, and  $\operatorname{erfc}$  is the

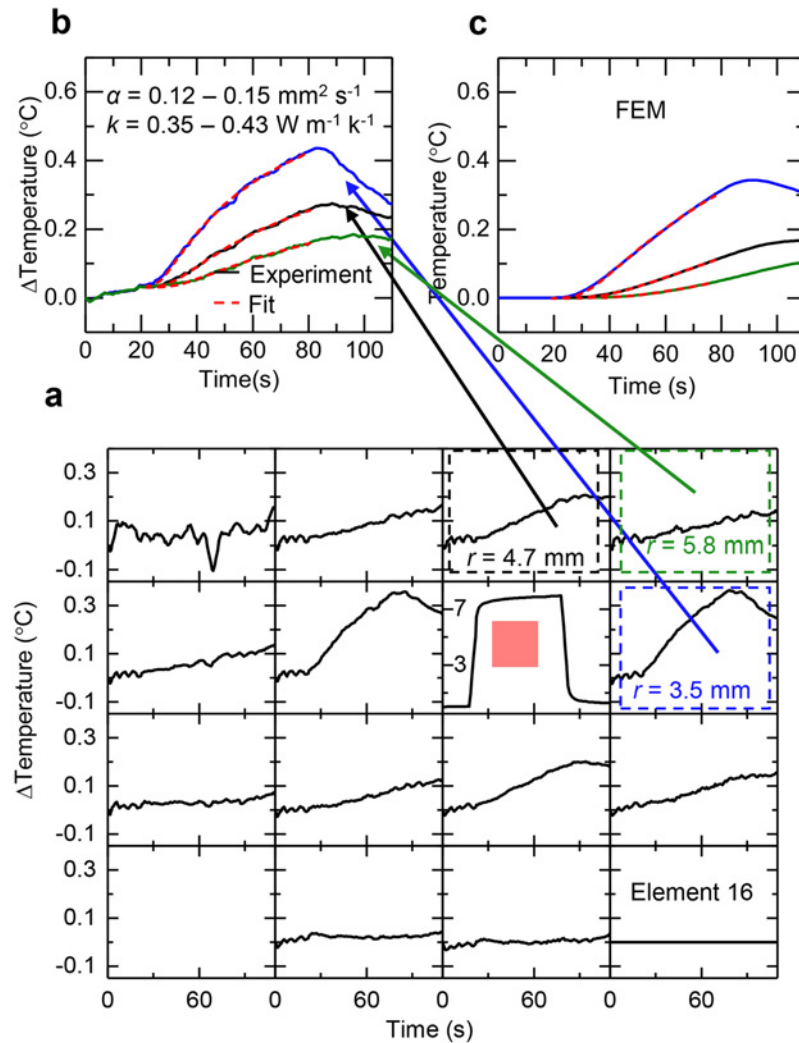


**Fig 8. Spatial mapping of thermal transport associated with low level heating on the surface of the skin.** (a) Spatial map of the changes in temperature at each sensor (i.e. element) in the array. The data processing uses an adjacent-average filter (window size = 8 s) and normalization to Element 16. The red highlight and colored boxes represent the elements boxed in the same colors in Fig. 1b. (b) Change in temperature at elements 3.5 mm away (blue), 4.7 mm away (black) and 5.8 mm away (red) from element responsible for thermal actuation. The solid and dashed lines represent experimental data and best fit calculations, with  $k \sim 0.35\text{--}0.43 \text{ W m}^{-1} \text{ K}^{-1}$  and  $\alpha \sim 0.12\text{--}0.15 \text{ mm}^2 \text{ s}^{-1}$ . (c) Results of finite element modelling of an array on a cheek, in the same arrangement as b.

doi:10.1371/journal.pone.0118131.g008

complementary error function.  $A_l$  is a parameter that accounts for details associated with the multilayered geometry of the device; its value is calibrated through measurements of materials with known thermal properties similar to those of the skin (water, ethylene glycol and polydimethylsiloxane).  $r(t)$  represents the effective distance of the sensor from the heating element and takes the form of a time dependent function that accounts for the finite spatial area of the sensing element (S1 Notes 6).  $k_{skin}$  and  $\alpha_{skin}$  can be determined in an iterative process similar to that used in equation (1). The treatment of  $r$  causes a maximum relative error of  $<2\%$  in the determination of  $k_{skin}$  and  $\alpha_{skin}$  compared to those values determined by integrating equation (3) over its area at each time point (S1 Notes 6). Representative results for different sensors appear in Fig. 8b. Finite element modeling (FEM) of the full device construct on a bilayer model

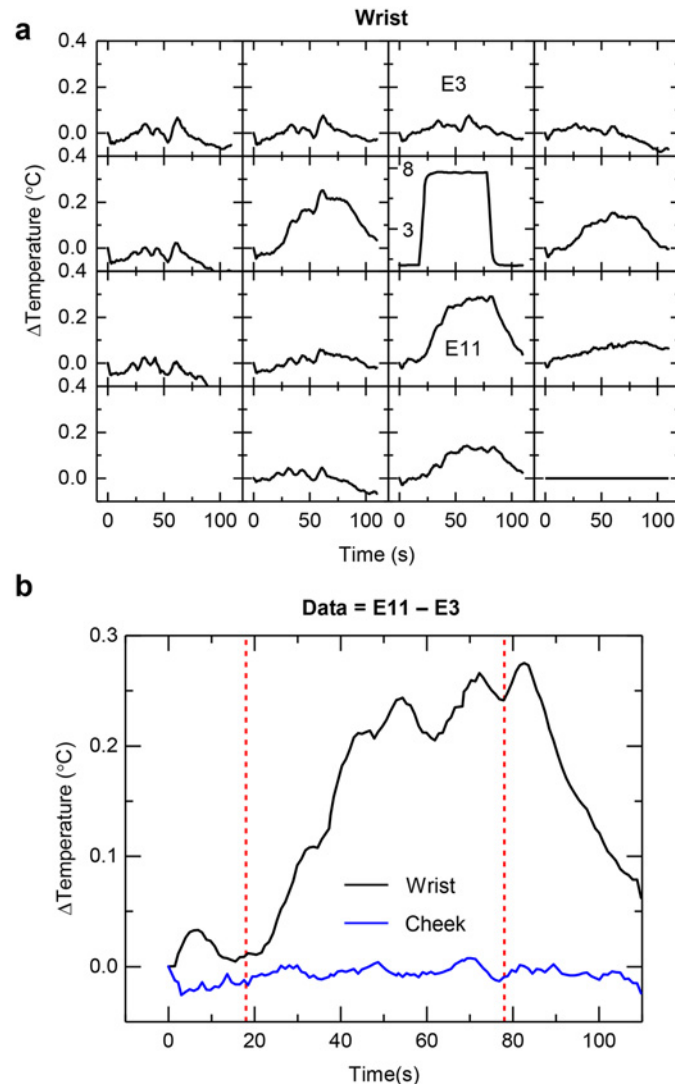


**Fig 9. Anisotropic convective effects associated with near surface blood flow.** (a) Spatial map of changes in temperature at each element for a device located at the volar aspect of the wrist. The position of the thermal actuator coincides with a large vein. (b) Difference in temperature between element 11 (E11) and element 3 (E3). The results show effects of anisotropic heat flow in the wrist, compared to isotropic distributions typically observed on a region of the body such as the cheek. The vertical red dashed lines correspond to initiation and termination of heating, respectively.

doi:10.1371/journal.pone.0118131.g009

of the skin yields temperature profiles (Fig. 8c) that closely match those observed in experiment. This measurement configuration provides additional information beyond that determined in equation (1) in the form of anisotropy in heat transport, at the expense of precision in the determination of thermal properties. Fig. 8 is an example of a skin area where the heat transport is strongly isotropic, while Fig. 9 illustrates the spatial changes in thermal transport on an area of skin with a significant anisotropic component to heat transport. Convective effects associated with blood that flows through vessels near the skin surface can induce in-plane, directional anisotropies in heat transport characteristics. Fig. 9 illustrates the effect when a device mounted on the volar aspect of the wrist includes a thermal actuator located over a near surface vein. The spatiotemporal temperature map in Fig. 9a shows a significantly larger

increase in temperature at the sensor located downstream (more proximal to the body, labeled E11) from the actuator, compared the one upstream (more distal to the body, labeled E3), relative to the direction of blood flow. Fig. 9b highlights one method to quantitatively assess the anisotropy in thermal flow. Here, the response of sensor E3 is subtracted from that of sensor E11 (sensors E3 and E11 are equidistant from the heating element, arranged on opposing sides of the heater) for the case on the wrist, which shows strong anisotropy due to blood flow, and for the case of isotropic data from a representative case on the cheek. The degree of anisotropic transport varies in strength over the twenty-five subjects due to differences in the locations and sizes of blood vessels and their associated flow properties. Such measurement capabilities have relevance in the determination of cardiovascular health, through inferred measurements of blood flow, both naturally and in response to stimuli such as temporary occlusion.

## Discussion

In summary, the work reported here reveals intrinsic thermal transport properties of the skin, including relationships to vascularization, blood flow, stratum corneum thickness and hydration level, made possible by expanded capabilities in soft ultrathin, non-invasive measurement systems that offer clear advantages compared to traditional approaches. As a demonstration of the new, *in vivo* measurement capabilities enabled by the device presented here, a clear relationship between skin hydration and *in vivo* thermal transport properties is shown across six body locations on twenty-five subjects. The data also reveal that the *in vivo* thermal transport properties of skin are not uniquely a function of hydration, but are also influenced by the structural makeup of the skin, as well as local blood flow characteristics. Obtaining similar data with alternative measurement techniques would require either expensive and complex optical thermography and laser heating systems, or bulky single-point probes that can have undesired effects on the skin properties of interest due the pressure that must be applied to skin when measured *in vivo*. The device and data presented here provide a foundational step for a new approach to the measurement of *in vivo* skin thermal properties, as well as new statistical data about the correlations between skin thermal transport properties, and skin hydration and structural makeup. Immediate further opportunities include use in studies of dermatological diseases, such as melanoma, rosacea and hyperpigmentation and their progression over time. The same techniques also offer ability to examine the effectiveness of dermatologically active compounds. Developments in wireless technology will provide a path to continuous monitoring of skin properties and function using these concepts.

## Methods

### Fabrication of Epidermal Thermal Sensing Array

Fabrication begins with a 3" Si wafer coated with a 200 nm layer of poly(methyl methacrylate), followed by 1  $\mu\text{m}$  of polyimide. Photolithographic patterning of a bilayer of Cr (6 nm)/Au (75 nm) deposited by electron beam evaporation defines the sensing/heating elements. A second multilayer of Ti (10 nm)/Cu (500 nm)/Ti (10 nm)/Au (25 nm), lithographically patterned, forms the connections to sensing/heating elements and non-oxidizing bonding locations for external electrical connection. A second layer of polyimide (1  $\mu\text{m}$ ) places the sensing/heating elements in the neutral mechanical plane and provides electrical insulation and mechanical strain isolation. Reactive ion etching of the polyimide defines the mesh layout of the array and exposes the bonding locations. A water-soluble tape (5414, 3M, USA) enables removal of the mesh layout from the Si wafer, to expose its back surface for deposition of Ti (3 nm)/SiO<sub>2</sub> (30 nm) by electron beam evaporation. Transfer to a thin silicone layer (5  $\mu\text{m}$ ; Ecoflex, Smooth-On, USA) spin-cast onto a glass slide, surface treated to reduce adhesion of the

silicone, results in the formation of strong bonds due to condensation reactions between exposed hydroxyl groups on and the SiO<sub>2</sub> and silicone. Immersion in warm water allows removal of the tape. A thin (100 μm), flexible, conductive cable (HST-9805–210; Elform, USA) bonded with heat and pressure to contacting pads at the periphery serves as a connection to external electronics. A final layer of silicone (70 μm) in combination with a frame of medical tape (Ease Release, 3M, USA) provides sufficient mechanical support to allow repeated (hundreds of times) use of a single device.

## Data Acquisition for Epidermal Thermal Sensing Array

The epidermal thermal sensing array is connected to external data acquisition electronics via a thin (100 μm) silver ink/polymer composite cable (HST-9805–210; Elform, USA). Resistance and voltage values across sensor/actuator elements are recorded by a USB-powered digital multimeter (USB-4065; National Instruments, USA). In order to heat elements, controlled current is supplied by a DC current source (6220 DC Current Source; Keithley, USA). The temperature during heating is monitored by recording the voltage across the heating element while receiving constant current input. The sensors are time-multiplexed via a USB-powered multiplexing circuit (U802; LedgeStone Technologies, USA).

## Experiments on Human Subjects

The volunteers consisted of healthy females, age between 18 and 45 years old, with healthy, intact skin of type II–IV according to the Fitzpatrick classification, recruited by Stephens & Associates, TX, USA. Approval by Stephens & Associates IRB: Protocol No. C14-D100 (ACR/TEMP/1416). Subjects provided written consent. The six investigational areas included the cheek, volar forearm, dorsal forearm, volar wrist, palm, and heel. Each subject acclimated to room temperature for 15 min immediately prior to measurement. The investigational areas were then gently cleaned with isopropyl alcohol, water, and dried with a swab to avoid skin irritation. Pictures were taken before and after the experimental procedures. SC hydration measurements used a 3 Cutometer MPA 580 (Courage + Khazaka Electronics GmbH). Skin temperature was evaluated using a handheld IR thermometer (DermaTemp, Exergen Co., USA). Calibration of the experimental measurement system introduced here occurred at a single temperature point (room temperature). Evaluations involved lamination of the device onto the investigational area, collection of relevant data, followed by removal. Three additional corneometer readings were then collected, followed by measurements by optical coherence tomography (VivoSight, Michelson Diagnostics, UK). The individual pictured in [Fig. 1](#) has given written informed consent (as outlined in the PLOS consent form) to publish these case details.

## Statistical Analyses

Box plot representations (SAS statistical software release 9.3, SAS Institute Inc., Cary, NC, USA) illustrate variables and trends by body location. The pairwise Pearson correlation coefficients were displayed as tables, scatterplot matrices, or heat map representations using JMP statistical software release 10.0 (JMP is a trademark of SAS Institute). Principal Component Analysis serve as a global multivariate approach with a biplot representation of individuals and descriptors (SIMCA statistical software release 13.0, UMETRICS, Umeå, Sweden).

## Supporting Information

**S1 Notes. Supplementary Notes 1–6: Supporting text, figures and tables.**  
(PDF)

**S1 Fig. Device construction and temperature comparison to IR measurements.** (a) Optical image of 4x4 thermal sensing array, showing the bonding location of the thin, flexible cable (ACF connection). (b) Magnified image of a single sensor/actuator element, showing the 10  $\mu\text{m}$  wide, serpentine configuration. (c) Cross-sectional schematic showing the device layout on skin. (d) Comparison of temperature device readings on six body locations on each of twenty-five subjects, as compared to IR measurements. Pearson correlation coefficient = 0.98. (TIF)

**S2 Fig. Representative photographs of each body location before, during, and after measurements.** Images show each body location before application of the thermal sensing array, with the device applied to skin during heating applications for thermal measurements, and then after device removal. No irritation is observed as a result of heating, or wearing the device. Body locations are (a) cheek, (b) volar forearm, (c) dorsal forearm, (d) wrist, (e) palm, and (f) heel. (TIF)

**S3 Fig. Temperature variations across body locations.** (a) Variation in temperature data between different subjects on different body locations for thermal sensing array (blue) and IR thermometer (red). (b) Inter- and intra-subject variance for the thermal sensing array and IR thermometer. (TIF)

**S4 Fig. Temperature variations across body locations for each subject.** Variation in temperature data between different subjects on different body locations for thermal sensing array (blue) and IR thermometer (red). (TIF)

**S5 Fig. Analysis of fitting process sensitivity with experimental error.** (a) Experimental precision fitting error analysis of representative *in vivo* data on a human heel. Experimental error range is given by 3x the standard deviation of temperature readings from the mean. (b) Experimental accuracy fitting error analysis of representative *in vivo* data on a human heel and (c) a human cheek. Experimental error range is given by the 95% confidence interval of temperature readings due to calibration errors. (TIF)

**S6 Fig. Experimental determination of measurement probing depth.** Measured thermal conductivities by the thermal sensing array for different thickness of a silicone with thermal properties similar to skin (Sylgard 170, Dow Corning, USA;  $k = 0.39 \text{ W m}^{-1} \text{ K}^{-1}$ ,  $\rho = 1370 \text{ kg m}^{-3}$ ) on copper. The measured thermal conductivity rises rapidly when the silicone layer becomes thinner than the probing depth, which is given by Eq. 2 to be approximately 0.5 mm. (TIF)

**S7 Fig. Solutions for  $r(t)$ .** Numerically determined solutions for  $r(t)$  over the appropriate measurement time, determined using  $k = 0.35 \text{ W m}^{-1} \text{ K}^{-1}$  and  $\alpha = 0.15 \text{ mm}^2 \text{ s}^{-1}$ , for (a)  $r = \sim 3.5 \text{ mm}$ , (b)  $r = \sim 4.7 \text{ mm}$ , and (c)  $r = \sim 5.8 \text{ mm}$ . (d) Example temperature rise solutions for a sensor  $\sim 3.5 \text{ mm}$  away using the integrated solution of Eq. S5,  $r(t)$  given in a with Eq. S6, and various time independent values of  $r$  with Eq. S6.  $r(t)$  gives the smallest discrepancy with Eq. S5 at  $<1\%$ , and time independent average values of  $r$  give discrepancies  $<5\%$ . (TIF)

**S8 Fig. Principle component analysis.** Boxplot representation of principal components by body location, and their corresponding relation to measured parameters. (a) Box plots and

correlation weights of the first principal component, (b) the second principal component and (c) the third principal component.

(TIF)

**S1 Table. Supplementary Table Pearson Correlation coefficients for the correlation analyses (Figs. 4–6).**

(TIF)

## Acknowledgments

We thank Adam Meekings and Michelson Diagnostics for discussions related to OCT image analysis, Dr. Giles Spenlehauer for discussions related to skin temperature studies and Dr. Thomas Stephens, Dr. Lily Jiang and Trang Nguyen for subject recruitment and assistance with clinical study organization. Research was supported by L'Oréal Research & Innovation, the Materials Research Laboratory and Center for Microanalysis of Materials at the University of Illinois at Urbana-Champaign.

## Author Contributions

Conceived and designed the experiments: RCW RMP MM GB JAR. Performed the experiments: RCW RMP JA JK AL NHC VM. Analyzed the data: RCW RMP PB JN. Contributed reagents/materials/analysis tools: RCW RMP PB MM VM. Wrote the paper: RCW RMP PB JN GB JAR.

## References

1. Graffe KVD (2001) Human Anatomy: McGraw Hill.
2. El-Brawany MA, Nassiri DK, Terhaar G, Shaw A, Rivens I, et al. (2009) Measurement of thermal and ultrasonic properties of some biological tissues. *Journal of Medical Engineering and Technology* 33: 249–256. doi: [10.1080/03091900802451265](https://doi.org/10.1080/03091900802451265) PMID: [19340696](https://pubmed.ncbi.nlm.nih.gov/19340696/)
3. Werner U, Giese K, Sennhenn B, Plamann K, Kolmel K (1992) Measurement of the thermal diffusivity of human epidermis by studying thermal wave propagation. *Phys Med Biol* 37: 21–35. PMID: [1741425](https://pubmed.ncbi.nlm.nih.gov/1741425/)
4. Togawa T, Saito H (1994) Non-contact imaging of thermal properties of the skin. *Physiological Measurement* 15: 291–298. PMID: [7994207](https://pubmed.ncbi.nlm.nih.gov/7994207/)
5. Ducharme MB, Tikuisis P (1991) In vivo thermal conductivity of the human forearm tissues. *Journal of Applied Physiology* 70: 2682–2690. PMID: [1885465](https://pubmed.ncbi.nlm.nih.gov/1885465/)
6. Jin C, He Z, Zhang S, Qi M, Sun Z, et al. (2012) A feasible method for measuring the blood flow velocity in superficial artery based on the laser induced dynamic thermography. *Infrared Physics and Technology* 55: 462–468.
7. Arnaud F, Delhomme G, Dittmar A, Girard P, Netchiporouk L, et al. (1994) A micro thermal diffusion sensor for non-invasive skin characterization. *Sensors and Actuators: A Physical* 41: 240–243.
8. Raamat R, Jagomägi K, Kingisepp PH (2002) Simultaneous recording of fingertip skin blood flow changes by multiprobe laser Doppler flowmetry and frequency-corrected thermal clearance. *Microvasc Res* 64: 214–219. PMID: [12204645](https://pubmed.ncbi.nlm.nih.gov/12204645/)
9. Kim DH, Lu NS, Ma R, Kim YS, Kim RH, et al. (2011) Epidermal Electronics. *Science* 333: 838–843. doi: [10.1126/science.1206157](https://doi.org/10.1126/science.1206157) PMID: [21836009](https://pubmed.ncbi.nlm.nih.gov/21836009/)
10. Webb RC, Bonifas AP, Behnaz A, Zhang YH, Yu KJ, et al. (2013) Ultrathin conformal devices for precise and continuous thermal characterization of human skin. *Nature Materials* 12: 938–944. doi: [10.1038/nmat3755](https://doi.org/10.1038/nmat3755) PMID: [24037122](https://pubmed.ncbi.nlm.nih.gov/24037122/)
11. Wang S, Li M, Wu J, Kim D-H, Lu N, et al. (2012) Mechanics of Epidermal Electronics. *Journal of Applied Mechanics* 79: 031022–031022.
12. Huang X, Cheng H, Chen K, Zhang Y, Zhang Y, et al. (2013) Epidermal impedance sensing sheets for precision hydration assessment and spatial mapping. *IEEE Trans Biomed Eng* 60: 2848–2857. doi: [10.1109/TBME.2013.2264879](https://doi.org/10.1109/TBME.2013.2264879) PMID: [23739778](https://pubmed.ncbi.nlm.nih.gov/23739778/)
13. Kaltenbrunner M, Sekitani T, Reeder J, Yokota T, Kuribara K, et al. (2013) An ultra-lightweight design for imperceptible plastic electronics. *Nature* 499: 458–463. doi: [10.1038/nature12314](https://doi.org/10.1038/nature12314) PMID: [23887430](https://pubmed.ncbi.nlm.nih.gov/23887430/)

14. Someya T, Kato Y, Sekitani T, Iba S, Noguchi Y, et al. (2005) Conformable, flexible, large-area networks of pressure and thermal sensors with organic transistor active matrixes. *Proc Natl Acad Sci U S A* 102: 12321–12325. PMID: [16107541](#)
15. Mannsfeld SC, Tee BC, Stoltenberg RM, Chen CV, Barman S, et al. (2010) Highly sensitive flexible pressure sensors with microstructured rubber dielectric layers. *Nat Mater* 9: 859–864. doi: [10.1038/nmat2834](#) PMID: [20835231](#)
16. Lacour SP, Jones J, Suo Z, Wagner S (2004) Design and performance of thin metal film interconnects for skin-like electronic circuits. *Ieee Electron Device Letters* 25: 179–181.
17. Sun JY, Lu NS, Yoon J, Oh KH, Suo ZG, et al. (2009) Inorganic islands on a highly stretchable polyimide substrate. *Journal of Materials Research* 24: 3338–3342.
18. Li T, Huang ZY, Suo Z, Lacour SP, Wagner S (2004) Stretchability of thin metal films on elastomer substrates. *Applied Physics Letters* 85: 3435–3437.
19. Carslaw HS, Jaeger JC (1959) *Conduction of heat in solids*. Oxford,: Clarendon Press. 510 p. p.
20. Gustafsson SE (1991) Transient plane source techniques for thermal conductivity and thermal diffusivity measurements of solid materials. *Review of Scientific Instruments* 62: 797–804.
21. Robertson K, Rees JL (2010) Variation in epidermal morphology in human skin at different body sites as measured by reflectance confocal microscopy. *Acta Derm Venereol* 90: 368–373. doi: [10.2340/00015555-0875](#) PMID: [20574601](#)
22. Egawa M, Hirao T, Takahashi M (2007) In vivo estimation of stratum corneum thickness from water concentration profiles obtained with Raman spectroscopy. *Acta Derm Venereol* 87: 4–8. PMID: [17225007](#)
23. Bohling A, Bielfeldt S, Himmelmann A, Keskin M, Wilhelm KP (2014) Comparison of the stratum corneum thickness measured in vivo with confocal Raman spectroscopy and confocal reflectance microscopy. *Skin Res Technol* 20: 50–57. doi: [10.1111/srt.12082](#) PMID: [23909688](#)

**Supplementary Information for:**

**Thermal Transport Characteristics of Human Skin Measured In Vivo Using Ultrathin Conformal Arrays of Thermal Sensors and Actuators**

R. Chad Webb<sup>1,†</sup>, Rafal M. Pielak<sup>2,†</sup>, Philippe Bastien<sup>3</sup>, Joshua Ayers<sup>1</sup>, Juha Niittynen<sup>4</sup>, Jonas Kurniawan<sup>1</sup>, Megan Manco<sup>5</sup>, Athena Lin<sup>1</sup>, Nam Heon Cho<sup>1</sup>, Viktor Malyrchuk<sup>1</sup>, Guive Balooch<sup>2,6,\*</sup> and John A. Rogers<sup>1,\*</sup>

<sup>1</sup>*Frederick Seitz Materials Research Laboratory, Department of Materials Science and Engineering, University of Illinois at Urbana-Champaign, Urbana, IL 61801, USA*

<sup>2</sup>*L'Oréal California Research Center, 953 Indiana St. San Francisco, CA 94107*

<sup>3</sup>*L'Oréal Research and Innovation, 1 av. Eugène Schuller, 39601 Aulnay sous Bois, France*

<sup>4</sup>*Tampere University of Technology, Department of Electronics and Communication Engineering, Korkeakoulunkatu 3, P.O. Box 692, FI-33101 Tampere, Finland*

<sup>5</sup>*L'Oréal Early Clinical, 133 Terminal Ave. Clark, NJ 07066*

<sup>6</sup>*L'Oréal Digital Incubator, 133 Terminal Ave. Clark, NJ 07066*

†These authors contributed equally to this work

\*To whom correspondence should be addressed. Guive Balooch: gbalooch@rd.us.loreal.com, John A. Rogers: [jrogers@illinois.edu](mailto:jrogers@illinois.edu)

## **Supplementary Note 1: Fabrication procedure for ultrathin thermal sensing arrays**

### ***Prepare polymer base layers***

1. Clean a 3" Si wafer (Acetone, IPA -> Dry 5 min at 110 °C).
2. Spin coat with PMMA (poly(methyl methacrylate) 495 A2 (Microchem), spun at 3,000 rpm for 30 s.
3. Anneal at 180 °C for 1 min.
4. Spin coat with polyimide (PI, poly(pyromellitic dianhydride-co-4,4'-oxydianiline), amic acid solution, Sigma-Aldrich, spun at 4,000 rpm for 30 s).
5. Anneal at 110 °C for 30 s.
6. Anneal at 150 °C for 5 min.
7. Anneal at 250 °C under vacuum for 1 hr.

### ***Deposit first metallization***

8. E-beam 6/75 nm Cr/Au.
9. Pattern photoresist (PR; Clariant AZ5214, 3000 rpm, 30s) with 365 nm optical lithography through iron oxide mask (Karl Suss MJB3).  
Develop in aqueous base developer (MIF 327).
10. Etch Au with TFA Au etchant (Transene).
11. Etch Cr with CR-7 Cr Mask Etchant (Cyantek).
12. Remove PR w/ Acetone, IPA rinse.
13. Dry 5 min at 150 °C.

### ***Deposit second metallization***

14. E-beam 10/500/10/25 nm Ti/Cu/Ti/Au.
15. Pattern PR AZ5214.
16. Etch Au with TFA Au etchant.
17. Etch Ti with 6:1 Buffered Oxide Etchant.
18. Etch Cu with CE-100 etchant (Transene).
19. Etch Ti with 6:1 Buffered Oxide Etchant.
20. Remove PR w/ Acetone, IPA rinse.
21. Dry 5 min at 150 °C.

### ***Isolate entire device***

22. Spin coat with PI.
23. Anneal at 110 °C for 30 s.
24. Anneal at 150 °C for 5 min.
25. Anneal at 250 °C under vacuum for 1 hr.
26. Pattern photoresist (PR; Clariant AZ4620, 3000 rpm, 30s) with 365 nm optical lithography through iron oxide mask (Karl Suss MJB3).

Develop in aqueous base developer (AZ 400K diluted 1:3, AZ 400K:Water).  
27. RIE (150 mTorr, 20 sccm O<sub>2</sub>, 200 W, 20 min).

### ***Release and transfer***

28. Release w/ boiling Acetone.
29. Transfer to water-soluble tape (Wave Solder Tape, 5414, 3M).
30. E-beam 3/30 nm Ti/SiO<sub>2</sub>.
31. Transfer to ~10 μm silicone sheet (Ecoflex, Smooth-on Co.) coated on silanized glass slide.
32. Immerse in warm water to dissolve tape.
33. Immerse quickly in Chrome Mask Etchant to remove any remaining residue.
34. Bond thin, flexible cable (Elform, HST-9805-210) using hot iron with firm pressure.
35. Apply additional silicone (10-100 μm) by doctor blade
36. Apply silicone medical tape frame (Ease Release Tape, 3M).
37. Remove device.

In order to provide a more appropriate system for repeated clinical use, we improve upon our initially demonstrated system in several ways. First, an electron beam evaporated metallic stack of Ti/Cu/Ti/Au (10/500/10/25 nm) replaces the expensive Au interconnect wiring system. This system provides the desired low resistivity interconnects while using minimal Au as a contact material. Narrow line widths (10 μm) in the sensing/heating elements provide high resistance in a small spatial area, shown in Fig. S1b, minimizing undesired heating in interconnect wires. A thin layer of Ecoflex (smooth-on, ETC) polymer between the sensor/heater elements (Fig. S1c) and the skin improves the adhesion directly between the heating element and the skin, minimizing errors in thermal transients that may be caused by air gaps. Finally, a silicone adhesive based tape (Ease Release, 3M, USA) functions as a frame for the device, providing a flexible but robust mechanical support for repeated use over >100 applications (see Fig. S2 for images before, during, and after measurement on each body location in the clinical study). Finally, the data acquisition and control system is in the form of a low cost, USB-powered portable system for practical clinical use. High temperature resolution is achieved by the 22-bit digital multimeter (USB-4065, National Instruments, USA) and time-multiplexing is achieved by the use of a USB-powered, voltage isolated switch circuit (U802, Ledgestone Technologies LLC, USA).

### **Supplementary Note 2: Temperature measurements across all body locations**

In order to verify temperature accuracy, temperature recordings by the device array are compared to recordings by a commercial infrared thermometer (DermaTemp, Exergen Co., USA) on each body location (Fig. S1d). The temperature values correlate well (Pearson's correlation coefficient,  $R = 0.98$ , slope =  $0.95 \pm 0.02$ , intercept =  $2.5 \pm 0.5$ , standard errors), verifying the value of the device in the context of epidermal temperature

sensing across varied body locations, as demonstrated previously [1]. Average temperature variations between body locations are shown in Fig. S3, and temperature variations of measured on each body location on each subject are shown in Fig. S4.

### **Supplemental Note 3: Estimated error in fitting models for clinical study**

The fitting model described by equation (1) and Fig. 2 is used to determine thermal property data for the 150 body locations measured during the clinical study. In this fitting procedure, two parameters, thermal conductivity and thermal diffusivity, are fit simultaneously. We assess the potential error in this fitting procedure by fixing one of the parameters, and allowing the other to float to determine the best fit with experimental data. In order to determine the fixed parameter value, we initially conduct the fit with both parameters floating to determine the best fit with experimental data (Fig. S5, red dashed line). We then fix one parameter, with a relative error from the best fit value, and allow the second parameter to float to determine a new best fit. We increase the error introduced to the fixed parameter until the new best fit curve falls just outside the error range of the experimental data (Fig. S5; best fit curves after applying error shown as blue and green dashed line; error range of experimental data shaded in red). The error range associated with the precision (i.e. the sensitivity of measurements using the same device one measurement to the next) of experimental data (Fig. S4a) is given as  $\pm 0.04$  °C, which is  $>3\sigma$ , where  $\sigma = 0.013$ °C is the *in vivo* experimental standard deviation of error from the mean. This error analysis conducted on several sets of *in vivo* data from our clinical study results in 2-3% potential error in the value of  $k$  and 8% potential error in the value of  $\alpha$ , with representative analyses from the heel shown in Figs. S5a. Each *in vivo* measurement involves solutions to  $k$  and  $\alpha$  from each of fifteen sensors in the array. The average standard deviation across all body locations, excluding the dorsal forearm which has large deviations due to hair on some subjects, of all subjects is 6% ( $0.02 \text{ W m}^{-1} \text{ K}^{-1}$ ) and 9% ( $0.013 \text{ mm}^2 \text{ s}^{-1}$ ) for  $k$  and  $\alpha$  respectively.

The error range associated with the sensor accuracy (i.e. the reliability of measurements when using different devices on measurement to the next) of experimental data is given by the 95% confidence interval of the sensor calibration of temperature sensitivity. This error analysis conducted on several sets of *in vivo* data from our clinical study results in 4-5% potential error in the value of  $k$  and 15% potential error in the value of  $\alpha$ , with representative analyses from the heel and cheek shown in Figs. S5b and S5c respectively.

### **Supplemental Note 4: Error analysis of equation (1) approximations**

The algorithm used to calculate skin thermal transport properties from transient heating in individual elements, shown in equation (1), is a convenient approximation to the solution of the average temperature of a small square with finite dimensions during transient heating. The approximation in equation (1) assumes that the average

temperature in the square can be approximated by assuming a point heat source at the center of the square, and a temperature rise some distance  $A_2$  away from the point source. The iteration of equation (1) is computationally inexpensive, which allows for rapid computation of the data from each element in the array. The potential error associated with equation (1) is investigated by comparison to the more exact, and computationally expensive, solution given by Gustafsson [2]

$$\overline{\Delta T(\tau)} = \frac{P_0 H(\tau)}{4\pi^{\frac{1}{2}} b k} \quad (\text{S1})$$

where  $P_0$  is the power output of the heater,  $b$  is the half width of the square heating element (0.5 mm for the our device),  $k$  is the thermal conductivity,

$$\tau = \frac{t\alpha}{b^2} \quad (\text{S2})$$

where  $\alpha$  is the thermal diffusivity,  $t$  is time and

$$H(\tau) = \int_0^\tau dv \{ \text{erf}(v^{-1}) - \pi^{-1/2} v [1 - \exp(-v^{-2})] \}^2 \quad (\text{S3})$$

where  $\text{erf}$  is the error function given by

$$\text{erf}(x) = 2\pi^{-1/2} \int_0^x dv \exp(-v^2). \quad (\text{S4})$$

equation (S1) accounts for the finite spatial extent of the heater to determine the average measured temperature of the heater. However, iterating this solutions of equations (S1) – (S4) over the large body of data with the high frequency measurement of data across many elements in an array quickly becomes computationally intensive. In order to compare the error using equation (1), we compare the thermal properties,  $k$  and  $\alpha$ , determined on a representative dataset using equation (1) to those determined by the iteration procedure of equations (S1) – (S4), once calibrated with known calibration media (water and ethylene glycol). The average discrepancy between the two procedures in the solution for  $k$  and  $\alpha$  is 3% and 8%, respectively, which is within the previously described error ranges due to noise. These potential errors will manifest in the form of constant accuracy offset that will be consistent across all devices. As a result, these potential errors will not influence the precision between measurements, different devices or the resultant correlation statistics that of primary interest.

### **Supplemental Note 5: Estimation of measurement depth**

The measurement technique outlined by equation (1) results in thermal property values that are a weighted average of the values encountered through the depth of skin that is probed by the measurement. The measurement depth can be approximated by equation

(2), which results in a measurement depth of ~500-1000  $\mu\text{m}$  in skin. We verify this result experimentally by conducting measurements on varying thickness of a polymer, with thermal properties similar to skin (Sylgard 170, Dow Corning, USA), on a base substrate of copper. The copper acts a thermal ground plane that will result in rapidly increasing measured thermal properties as the measurement depth approaches the polymer thickness. The resultant measured thermal conductivities on various thicknesses of polymer on copper are shown in Fig. S6, and the measured thermal conductivities begin to rise rapidly at a polymer thickness of approximately 500  $\mu\text{m}$ .

### Supplemental Note 6: Error analysis of equation (3) approximations

The measurement configuration outlined by equation (3) and Fig. 8 assumes a discrete distance,  $r$ , away from a point source heater. The sensors in the array in use here have a finite aerial spatial extent of 1 mm x 1 mm, with <3  $\mu\text{m}$  thickness. The temperature increase recorded by a sensor corresponds to the average temperature increase over the sensor area. Assuming isotropic radial conduction, valid for cases without anisotropic convective transport due to blood, the average temperature across the sensor,  $\bar{T}$ , is approximately equal to the average temperature rise between points  $r_1$  and  $r_2$  away from a point source heater, given by

$$\bar{T} = \frac{\int_{r_1}^{r_2} \frac{Q}{2\pi r k_{skin}} \operatorname{erfc}\left(\frac{r\sqrt{\rho_{skin}c_{p,skin}}}{\sqrt{4k_{skin}t}}\right) dr}{r_2 - r_1} \quad (\text{S5})$$

where  $r_1$  and  $r_2$  are 1 mm apart and represent the distances of the sensor near and far edges, respectively, from the heater. equation (S5) can be approximated by

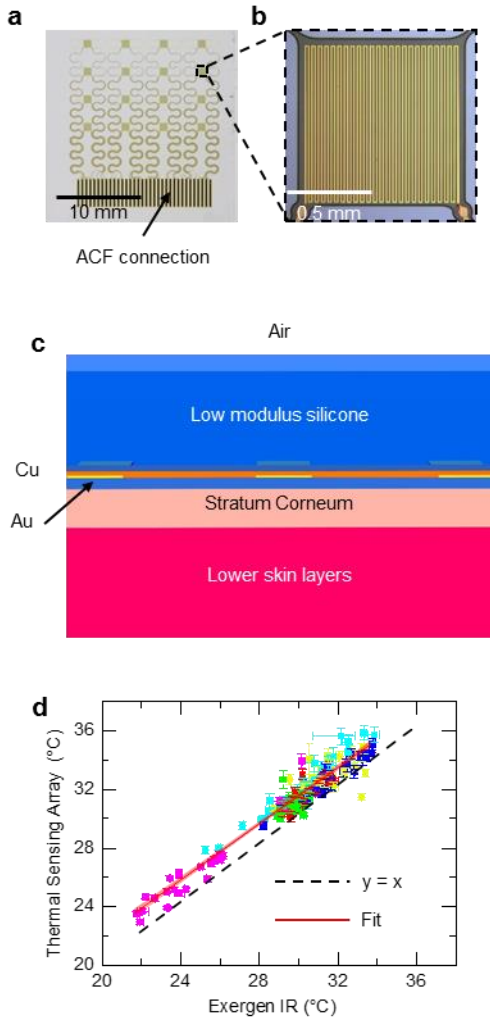
$$\bar{T} = \frac{Q}{2\pi r(t)k_{skin}} \operatorname{erfc}\left(\frac{r(t)\sqrt{\rho_{skin}c_{p,skin}}}{\sqrt{4k_{skin}t}}\right) \quad (\text{S6})$$

where the integral average over the sensor in equation (S5) has been replaced by  $r(t)$ , a time dependent characteristic distance.  $r(t)$  is determined numerically by setting equation (S5) equal to equation (S6). Specifically, equation (S5) is solved for a fixed  $k_{skin}$  and  $\rho_{skin}c_{p,skin}$ . equation (S6) is then solved in an iterative fashion to minimize the error between equation (S6) and equation (S5), where  $r(t)$  is allowed to vary, and  $k_{skin}$  and  $\rho_{skin}c_{p,skin}$  are fixed to the values used in the solution for equation (S5).  $k_{skin} = 0.35 \text{ W m}^{-1} \text{ K}^{-1}$  and  $\rho_{skin}c_{p,skin} = 2.33 \text{ J cm}^{-3} \text{ K}^{-1}$  are the approximate midpoint values of the *in vivo* data, and are used to establish  $r(t)$  for the three sensor distances of ~3.5 mm, ~4.7 mm, and ~5.8 mm.  $r(t)$  begins at a value near that of the distance between the heat source and nearest edge of the sensor, and rapidly approaches the mean sensor distance from the heater.  $r(t)$  is, more generally, a function of  $\rho_{skin}c_{p,skin}/k_{skin}$ , and the solutions of  $r(t)$  for  $k_{skin} = 0.35 \text{ W m}^{-1} \text{ K}^{-1}$  and  $\rho_{skin}c_{p,skin} = 2.33 \text{ J cm}^{-3} \text{ K}^{-1}$  are shown in Figs. S7A-C. While  $r(t)$  is a function of thermal properties as well as time, the  $r(t)$  values shown in Figs. S7a-c are

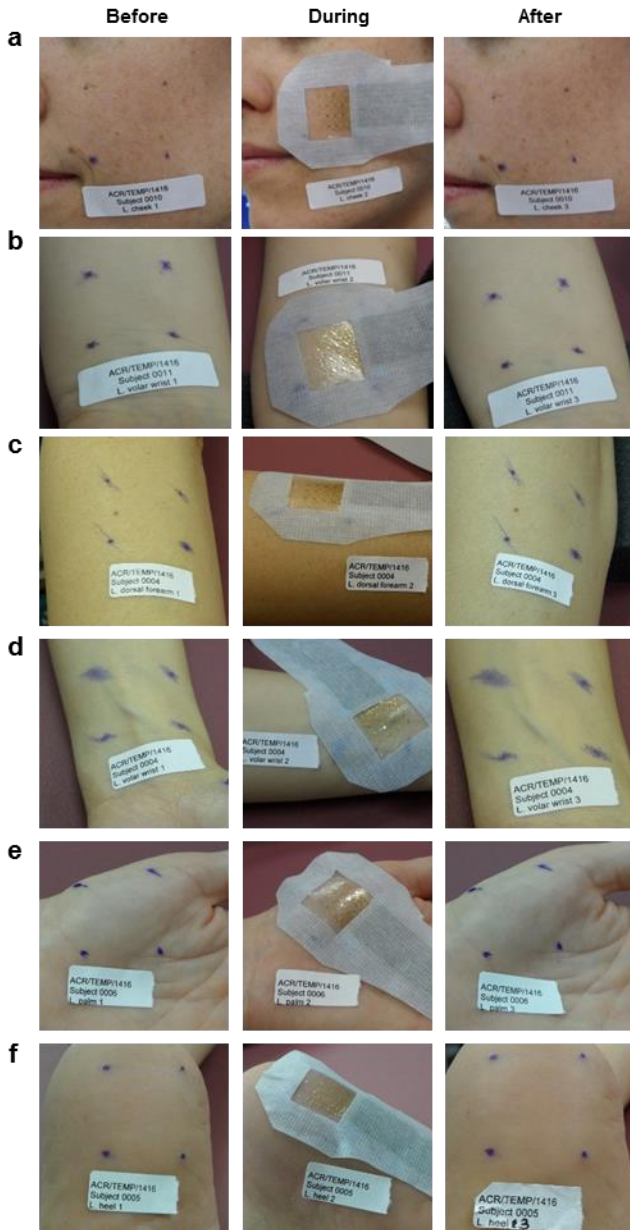
assumed to be reasonable approximations for all thermal properties encountered on skin *in vivo*. The error associated with this approximation can be estimated by determining  $r(t)$  for one set of thermal property values (the mid-range values of the *in vivo* data), and equation (S5) is solved for a set of thermal property values different from those used to determine  $r(t)$  (high-range values of the *in vivo* data). Equation (S6) is then solved, where  $r(t)$  is fixed and  $k_{skin}$  and  $\rho_{skin}C_{p,skin}$  are varied iteratively to minimize the error between equation (S6) and equation (S5). A typical result from this type of analysis is shown in Fig. S7d, along with the results determined by replacing  $r(t)$  with different time independent values (geometric mean, harmonic mean, and  $r_1$ ). The discrepancy between the results determined by equation (S5) and the approximation using  $r(t)$  with equation (S6) are found to be <1%. The still simpler solution using a single, time-independent value in place of  $r(t)$  are found to produce errors <5%, if chosen appropriately.

## References

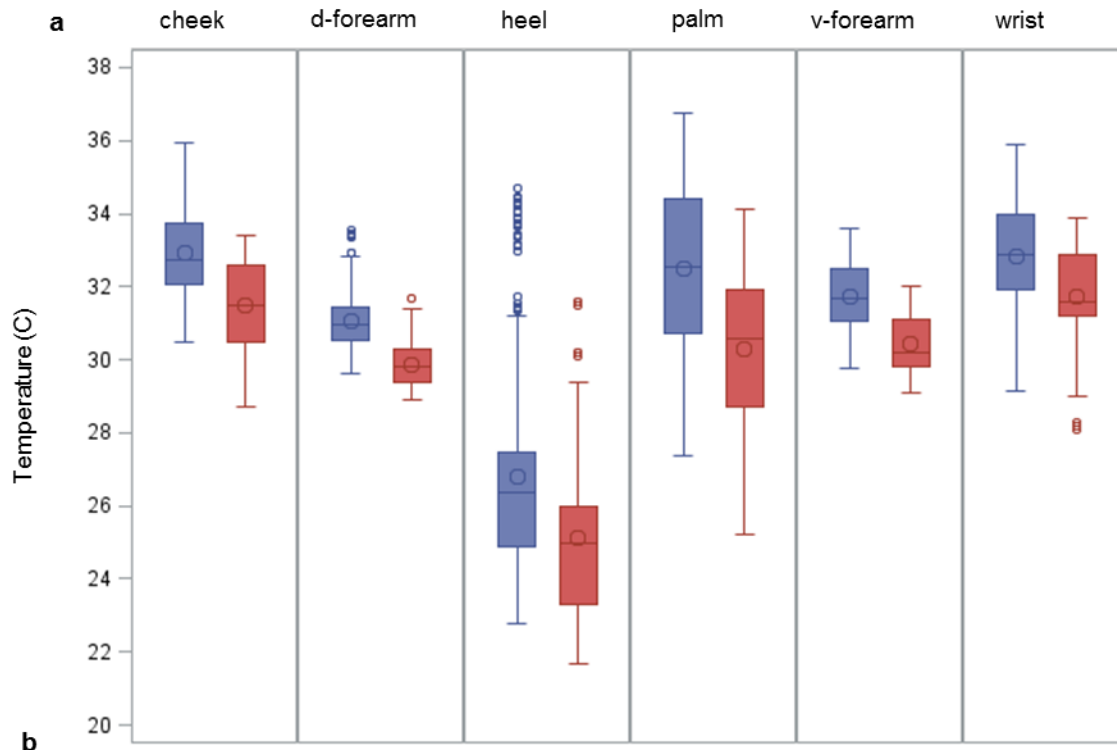
1. Webb RC, Bonifas AP, Behnaz A, Zhang YH, Yu KJ, et al. (2013) Ultrathin conformal devices for precise and continuous thermal characterization of human skin. *Nature Materials* 12: 938-944.
2. Gustafsson SE (1991) Transient plane source techniques for thermal conductivity and thermal diffusivity measurements of solid materials. *Review of Scientific Instruments* 62: 797-804.



**Supplemental Figure S1: Device construction and temperature comparison to IR measurements.** (a) Optical image of 4x4 thermal sensing array, showing the bonding location of the thin, flexible cable (ACF connection). (b) Magnified image of a single sensor/actuator element, showing the 10  $\mu\text{m}$  wide, serpentine configuration. (c) Cross-sectional schematic showing the device layout on skin. (d) Comparison of temperature device readings on six body locations on each of twenty-five subjects, as compared to IR measurements. Pearson correlation coefficient = 0.98.

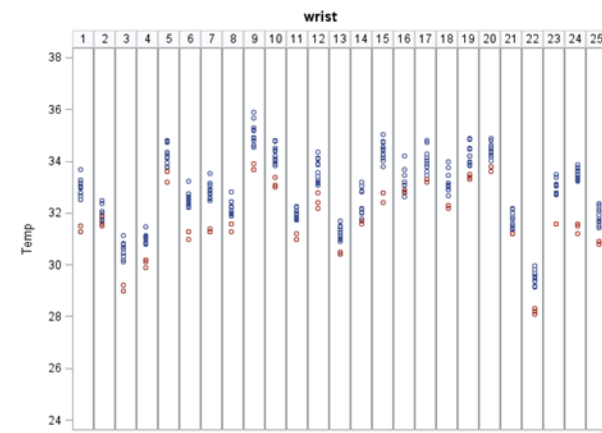
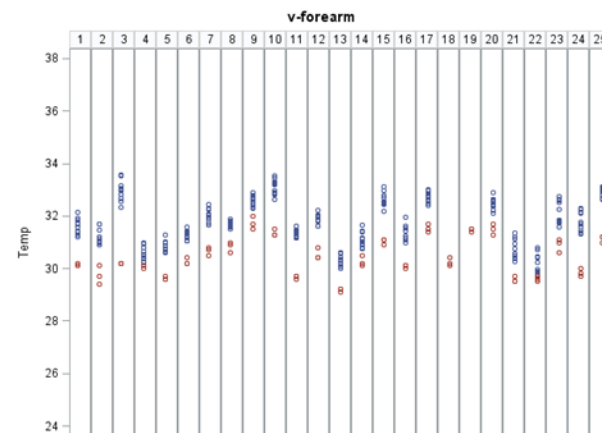
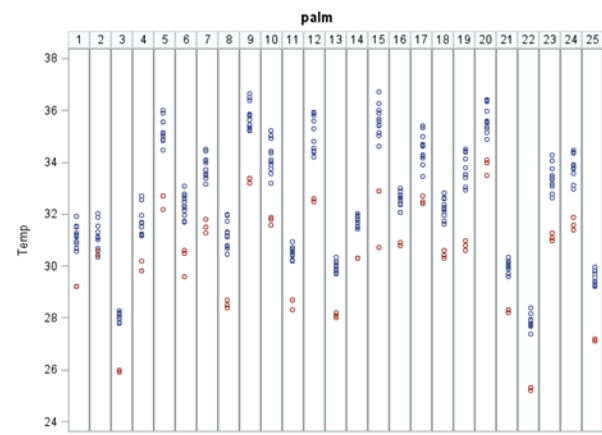
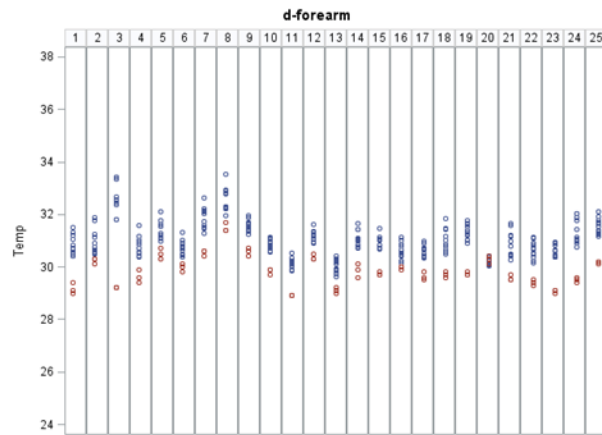
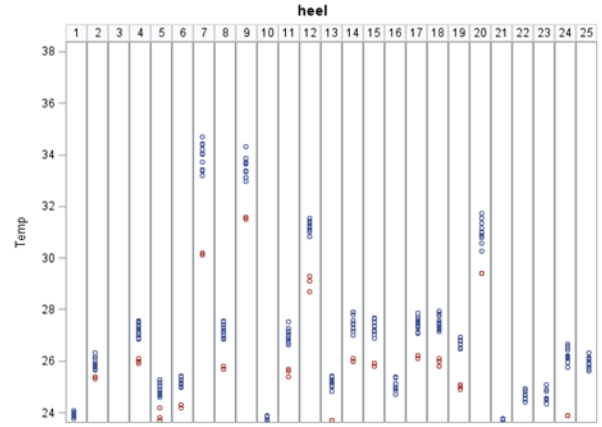
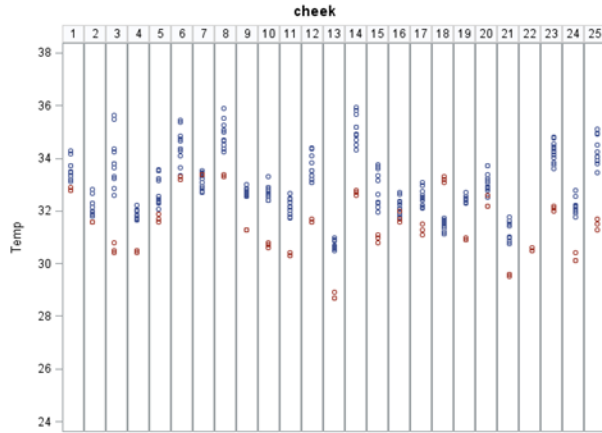


**Supplemental Figure S2: Representative photographs of each body location before, during, and after measurements.** Images show each body location before application of the thermal sensing array, with the device applied to skin during heating applications for thermal measurements, and then after device removal. No irritation is observed as a result of heating, or wearing the device. Body locations are (a) cheek, (b) volar forearm, (c) dorsal forearm, (d) wrist, (e) palm, and (f) heel.

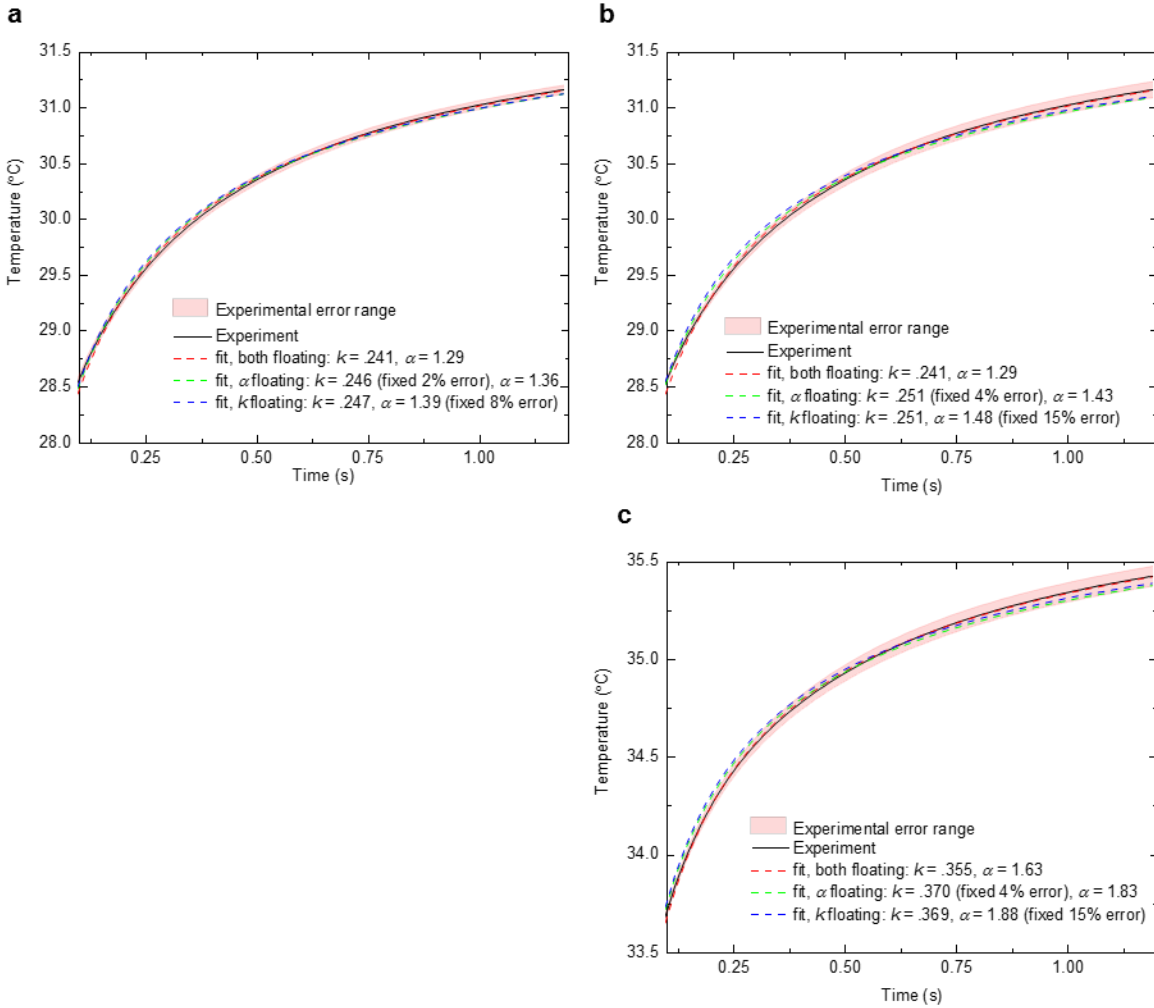


Thermal Sensing Array	Intersubject variance	Intrasubject variance
Cheek	1.31	0.19
d-Vorearm	0.40	0.12
Heel	8.34	0.06
Palm	5.43	0.21
v-Forearm	0.76	0.07
Wrist	1.88	0.12
IR		
Cheek	1.48	0.15
d-Vorearm	0.34	0.02
Heel	6.90	0.02
Palm	4.89	0.10
v-Forearm	0.53	0.03
Wrist	1.97	0.02

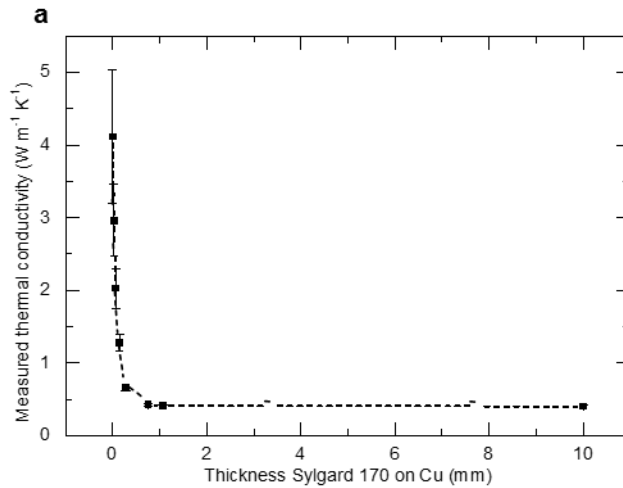
**Supplemental Figure S3: Temperature variations across body locations.** (a) Variation in temperature data between different subjects on different body locations for thermal sensing array (blue) and IR thermometer (red). (b) Inter- and intra-subject variance for the thermal sensing array and IR thermometer.



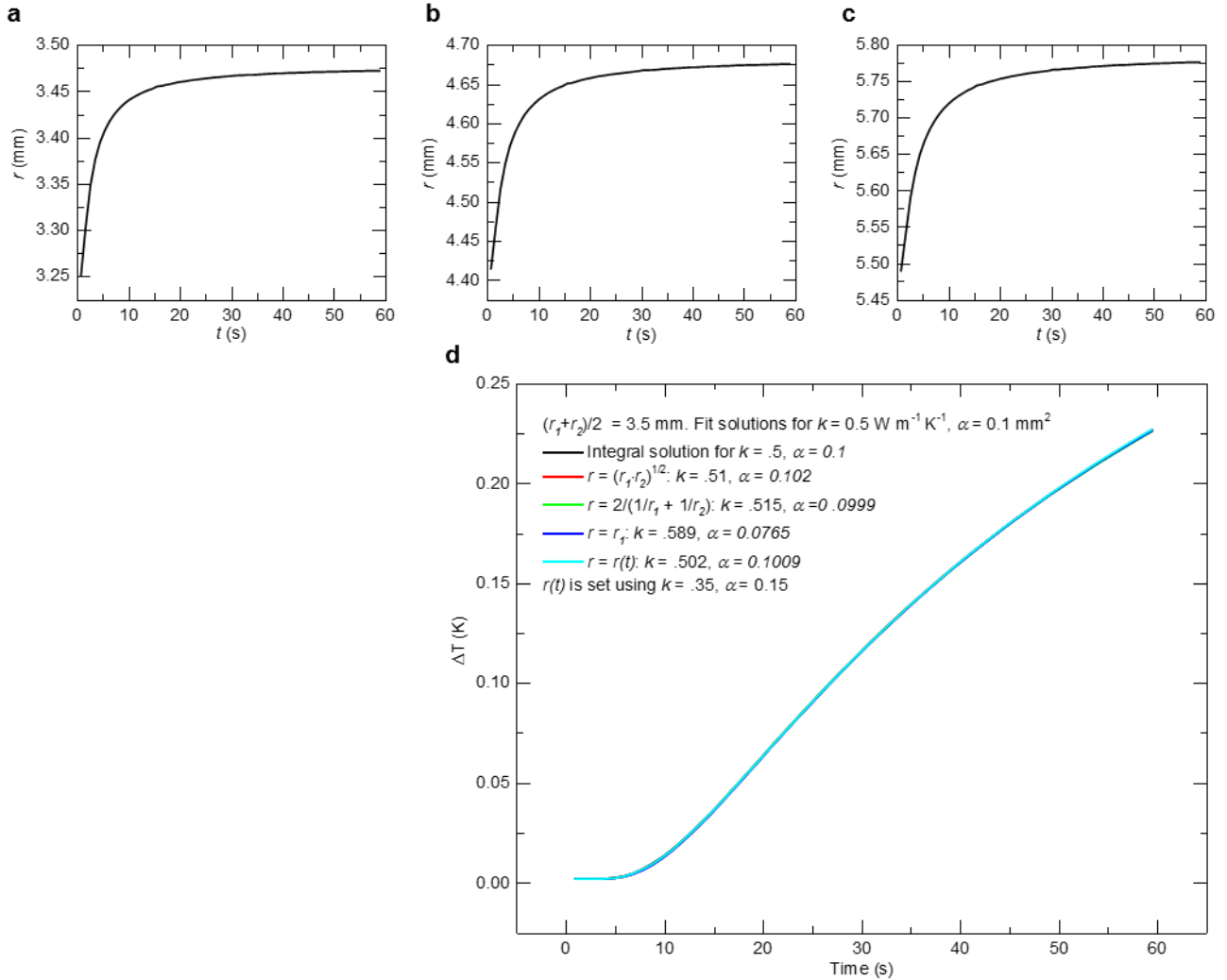
**Supplemental Figure S4: Temperature variations across body locations for each subject.** Variation in temperature data between different subjects on different body locations for thermal sensing array (blue) and IR thermometer (red).



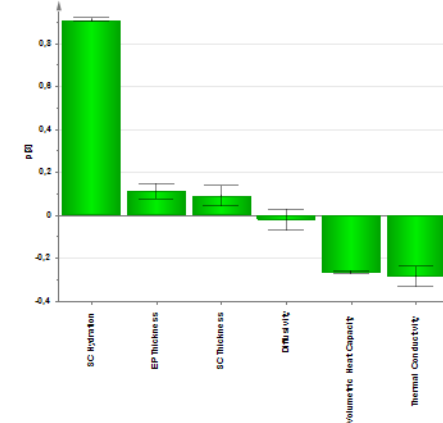
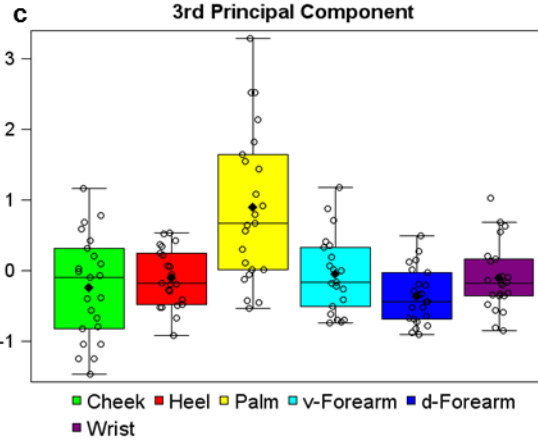
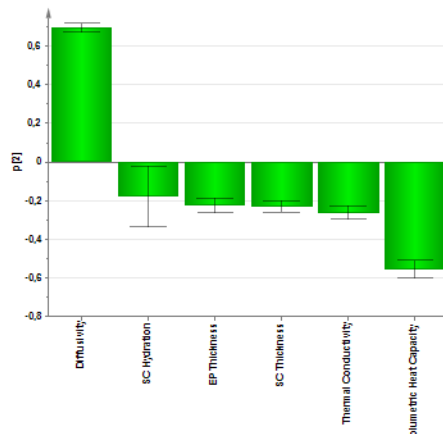
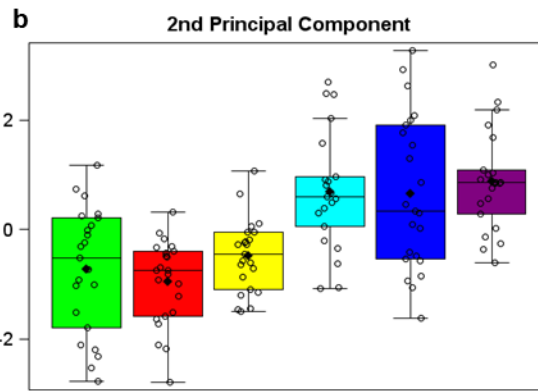
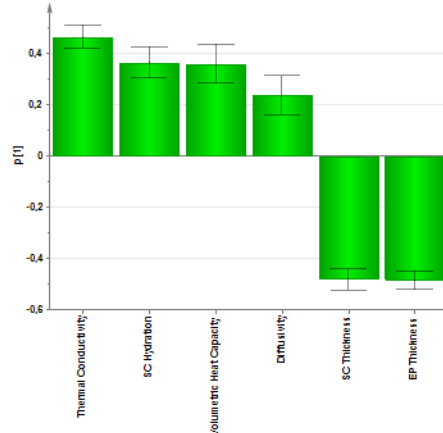
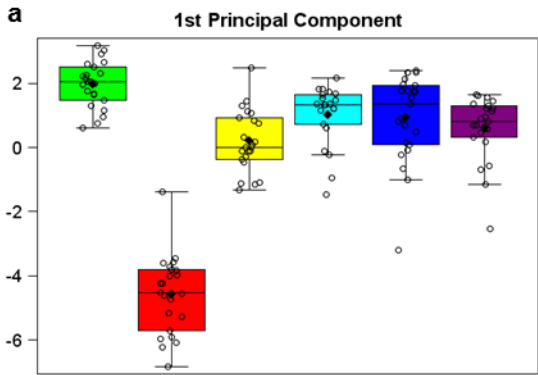
**Supplemental Figure S5: Analysis of fitting process sensitivity with experimental error.** (a) Experimental precision fitting error analysis of representative *in vivo* data on a human heel. Experimental error range is given by 3x the standard deviation of temperature readings from the mean. (b) Experimental accuracy fitting error analysis of representative *in vivo* data on a human heel and (c) a human cheek. Experimental error range is given by the 95% confidence interval of temperature readings due to calibration errors.



**Supplemental Figure S6: Experimental determination of measurement probing depth.** Measured thermal conductivities by the thermal sensing array for different thickness of a silicone with thermal properties similar to skin (Sylgard 170, Dow Corning, USA;  $k = 0.39 \text{ W m}^{-1} \text{ K}^{-1}$ ,  $\rho = 1370 \text{ kg m}^{-3}$ ) on copper. The measured thermal conductivity rises rapidly when the silicone layer becomes thinner than the probing depth, which is given by Eq. 2 to be approximately 0.5 mm.



**Supplemental Figure S7: Solutions for  $r(t)$ .** Numerically determined solutions for  $r(t)$  over the appropriate measurement time, determined using  $k = 0.35 \text{ W m}^{-1} \text{ K}^{-1}$  and  $\alpha = 0.15 \text{ mm}^2 \text{ s}^{-1}$ , for (a)  $r = \sim 3.5$  mm, (b)  $r = \sim 4.7$  mm, and (c)  $r = \sim 5.8$  mm. (d) Example temperature rise solutions for a sensor  $\sim 3.5$  mm away using the integrated solution of Eq. S5,  $r(t)$  given in a with Eq. S6, and various time independent values of  $r$  with Eq. S6.  $r(t)$  gives the smallest discrepancy with Eq. S5 at  $<1\%$ , and time independent average values of  $r$  give discrepancies  $<5\%$ .



**Supplemental Figure S8. Principle component analysis.** Boxplot representation of principal components by body location, and their corresponding relation to measured parameters. (a) Box plots and correlation weights of the first principal component, (b) the second principal component and (c) the third principal component.

## Multivariate

### Correlations

	SC Hydration	SC Thickness	EP Thickness	Thermal Conductivity	Volumetric Heat Capacity	Diffusivity
SC Hydration	1.0000	-0.5523	-0.5479	0.5779	0.5157	0.1376
SC Thickness	-0.5523	1.0000	0.9957	-0.7427	-0.4653	-0.6446
EP Thickness	-0.5479	0.9957	1.0000	-0.7567	-0.4775	-0.6465
Thermal Conductivity	0.5779	-0.7427	-0.7567	1.0000	0.9040	0.1774
Volumetric Heat Capacity	0.5157	-0.4653	-0.4775	0.9040	1.0000	-0.2551
Diffusivity	0.1376	-0.6446	-0.6465	0.1774	-0.2551	1.0000

There are 2 missing values. The correlations are estimated by REML method.

## Multivariate Location=cheek

### Correlations

	SC Hydration	SC Thickness	EP Thickness	Thermal Conductivity	Volumetric Heat Capacity	Diffusivity
SC Hydration	1.0000	0.0000	0.1456	0.1504	0.2395	-0.2964
SC Thickness	0.0000	0.0000	0.0000	0.0000	0.0000	0.0000
EP Thickness	0.1456	0.0000	1.0000	0.0876	0.1772	-0.2219
Thermal Conductivity	0.1504	0.0000	0.0876	1.0000	0.9418	-0.7469
Volumetric Heat Capacity	0.2395	0.0000	0.1772	0.9418	1.0000	-0.9247
Diffusivity	-0.2964	0.0000	-0.2219	-0.7469	-0.9247	1.0000

## Multivariate Location=d-forearm

### Correlations

	SC Hydration	SC Thickness	EP Thickness	Thermal Conductivity	Volumetric Heat Capacity	Diffusivity
SC Hydration	1.0000	0.0000	-0.0561	0.7388	0.7431	-0.5789
SC Thickness	0.0000	0.0000	0.0000	0.0000	0.0000	0.0000
EP Thickness	-0.0561	0.0000	1.0000	0.0376	0.0217	0.0334
Thermal Conductivity	0.7388	0.0000	0.0376	1.0000	0.9746	-0.7246
Volumetric Heat Capacity	0.7431	0.0000	0.0217	0.9746	1.0000	-0.8573
Diffusivity	-0.5789	0.0000	0.0334	-0.7246	-0.8573	1.0000

## Multivariate Location=heel

### Correlations

	SC Hydration	SC Thickness	EP Thickness	Thermal Conductivity	Volumetric Heat Capacity	Diffusivity
SC Hydration	1.0000	-0.6045	-0.6767	0.5433	0.3940	0.0653
SC Thickness	-0.6045	1.0000	0.9579	-0.4823	-0.3962	0.0620
EP Thickness	-0.6767	0.9579	1.0000	-0.5074	-0.4049	0.0434
Thermal Conductivity	0.5433	-0.4823	-0.5074	1.0000	0.9496	-0.5243
Volumetric Heat Capacity	0.3940	-0.3962	-0.4049	0.9496	1.0000	-0.7628
Diffusivity	0.0653	0.0620	0.0434	-0.5243	-0.7628	1.0000

## Multivariate Location=palm

### Correlations

	SC Hydration	SC Thickness	EP Thickness	Thermal Conductivity	Volumetric Heat Capacity	Diffusivity
SC Hydration	1.0000	-0.5413	-0.4691	0.5784	0.4066	0.1606
SC Thickness	-0.5413	1.0000	0.9145	-0.6861	-0.4179	-0.3327
EP Thickness	-0.4691	0.9145	1.0000	-0.5601	-0.3172	-0.3248
Thermal Conductivity	0.5784	-0.6861	-0.5601	1.0000	0.9013	-0.1981
Volumetric Heat Capacity	0.4066	-0.4179	-0.3172	0.9013	1.0000	-0.6021
Diffusivity	0.1606	-0.3327	-0.3248	-0.1981	-0.6021	1.0000

## Multivariate Location=v-forearm

### Correlations

	SC Hydration	SC Thickness	EP Thickness	Thermal Conductivity	Volumetric Heat Capacity	Diffusivity
SC Hydration	1.0000	1.0000	-0.0608	0.1426	0.1718	-0.1883
SC Thickness	1.0000	1.0000	-0.0608	0.1426	0.1718	-0.1883
EP Thickness	-0.0608	-0.0608	1.0000	-0.4181	-0.3845	0.2396
Thermal Conductivity	0.1426	0.1426	-0.4181	1.0000	0.9587	-0.6740
Volumetric Heat Capacity	0.1718	0.1718	-0.3845	0.9587	1.0000	-0.8546
Diffusivity	-0.1883	-0.1883	0.2396	-0.6740	-0.8546	1.0000

There are 2 missing values. The correlations are estimated by REML method.

## Multivariate Location=wrisk

### Correlations

	SC Hydration	SC Thickness	EP Thickness	Thermal Conductivity	Volumetric Heat Capacity	Diffusivity
SC Hydration	1.0000	0.0000	-0.2143	0.4363	0.4167	-0.2230
SC Thickness	0.0000	0.0000	0.0000	0.0000	0.0000	0.0000
EP Thickness	-0.2143	0.0000	1.0000	-0.1626	-0.0179	-0.3725
Thermal Conductivity	0.4363	0.0000	-0.1626	1.0000	0.9659	-0.4868
Volumetric Heat Capacity	0.4167	0.0000	-0.0179	0.9659	1.0000	-0.6934
Diffusivity	-0.2230	0.0000	-0.3725	-0.4868	-0.6934	1.0000

Supplemental Table 1. Pearson Correlation coefficients for the correlation analyses (Figs. 4-6).